Available online at www.sciencedirect.com
ScienceDirect
Combustion and Flame 148 (2007) 4–47
Combustion and Flame
www.elsevier.com/locate/combustflame

Origins of the deflagration-to-detonation transition in gas-phase combustion

Elaine S. Oran *, Vadim N. Gamezo

Laboratory for Computational Physics & Fluids Dynamics, US Naval Research Laboratory, Washington, DC 20375, USA

Received 2 February 2006; received in revised form 17 July 2006; accepted 25 July 2006

Abstract

This paper summarizes a 10-year theoretical and numerical effort to understand the deflagration-to-detonation transition (DDT). To simulate DDT from first principles, it is necessary to resolve the relevant scales ranging from the size of the system to the flame thickness, a range that can cover up to 12 orders of magnitude in real systems. This computational challenge resulted in the development of numerical algorithms for solving coupled partial and ordinary differential equations and a new method for adaptive mesh refinement to deal with multiscale phenomena. Insight into how, when, and where DDT occurs was obtained by analyzing a series of multidimensional numerical simulations of laboratory experiments designed to create a turbulent flame through a series of shock–flame interactions. The simulations showed that these interactions are important for creating the conditions in which DDT can occur. Flames enhance the strength of shocks passing through a turbulent flame brush and generate new shocks. In turn, shock interactions with flames create and drive the turbulence in flames. The turbulent flame itself does not undergo a transition, but it creates conditions in nearby unreacted material that lead to ignition centers, or "hot spots," which can then produce a detonation through the Zeldovich gradient mechanism involving gradients of reactivity. Obstacles and boundary layers, through their interactions with shocks and flames, help to create environments in which hot spots can develop. Other scenarios producing reactivity gradients that can lead to detonations include flame–flame interactions, turbulent mixing of hot products with reactant gases, and direct shock ignition. Major unresolved questions concern the properties of nonequilibrium, shock-driven turbulence, stochastic properties of ignition events, and the possibility of unconfined DDT.

Keywords: Deflagration; Detonation; DDT; Numerical simulation; Shock–flame interactions; Shock–flame–boundary layer interactions

Contents

---

* Corresponding author. Fax: +1 202 767 6260.
E-mail address: oran@lcp.nrl.navy.mil (E.S. Oran).

0010-2180/$ – see front matter Published by Elsevier Inc. on behalf of The Combustion Institute.
doi:10.1016/j.combustflame.2006.07.010

1. Introduction

This paper chronicles part of a scientific odyssey that resulted from a collaboration among members of a motley group consisting of combustion scientists and astrophysicists. This includes Alexei M. Khokhlov, J. Craig Wheeler, Geraint O. Thomas, and the authors. The question that drove this work was a particular combustion problem: *What are the physical mechanisms underlying the deflagration-to-detonation transition (DDT) in gaseous energetic mixtures?* DDT is a basic combustion problem that has been called one of the major unsolved problems in theoretical combustion theory. It also has important applications ranging from ensuring safe storage of fuels and explosives to deciphering some of the most fundamental issues in astrophysics and cosmology.

Our initial interest was motivated in part by practical combustion issues. Unwanted, uncontrolled DDT has enormous destructive potential. For example, it is an important topic in the safety and handling of energetic materials. Questions arise such as: *How can we avoid "accidental" explosions? How do we minimize the possibility of mine explosions? Is DDT related to engine knock?* Recently DDT has become important for new propulsion applications, and we ask questions such as *How do we optimize or control detonation initiation?* In addition, our interest in DDT is motivated by an astrophysical question: *How does a Type Ia supernova explode?* The underlying relations between these different types of problems are what has allowed this work to move forward.

A quantitative prediction of DDT in energetic gases is an extremely difficult scientific problem that requires information about the dynamics of interactions among flames, shocks, boundary layers, and turbulence. These highly nonlinear interactions involve a number of physical and chemical processes and occur over spatial scales that span many orders of magnitude. For laboratory systems, the flame thickness is typically 4 to 6 orders of magnitude smaller than the system size. The scales may differ by up to 10 orders of magnitude for hazardous industrial scenarios, and by up to 12 orders of magnitude for Type Ia supernovae.

But even a mere 6 orders of magnitude presented a formidable problem in 1996 when this project started. At that time, we estimated that the computational times needed for simulating a laboratory shock-tube system, in which we could hope to observe DDT, would be about 6 weeks for a 2D system and about 1000 years for a 3D system! All of this assumed that the computations were performed on a now-obsolete computer, the Connection Machine, that had a nearly optimal architecture for these types of computations, and we could find a machine with enough computer memory and available processors. These estimates were made for simulating a low-pressure acetylene–air system studied previously in a series of experiments at the University of Wales. Although a 6-week calculation might be possible for a very important problem, a 1000-year calculation is manifestly ridiculous. An application of Moore's Law[1] would say that the fastest way to do the calculation would be to wait twenty years until computers are much bigger and faster. With this assumption, a calculation that would take 1000 years now might take a few weeks then.

DDT in the laboratory has been observed in several types of experiments in chambers containing cold, unreacted, exothermic gases. These include creating a series of shock–flame interactions and igniting the mixture with a spark, a shock, or a hot turbulent jet. This paper focuses primarily on the scenario in which the primary initial interaction is that of an imposed shock and a laminar flame. We first describe the approach we used and then summarize what we have learned in the past 10 years using this approach. We also include more limited descriptions of simulations of shock-induced weak and strong ignition and analyze flame–turbulence interactions related to DDT in unconfined systems.

The approach we used combined theoretical analyses, experiments, and extensive numerical simulations. Theoretical work involved formulating theories that could be tested with simulations. It also involved developing appropriate submodels with just enough complexity to compute a DDT event. Experimental work involved designing appropriate experiments that showed trends and phenomena we could attempt to study with a simulation. Numerical aspects involved developing adaptive gridding algorithms, parallelization to obtain optimal performance, many resolution and convergence tests, and, finally, simulations of laboratory experiments to study mechanisms of DDT.

Our primary tool, however, was multidimensional, time-dependent numerical simulation of unsteady combustion using high-performance parallel computers. The objective of the simulations was to model DDT from "first principles," by which we mean to resolve all of the relevant scales, ranging from the laminar flame thickness to the size of the system. In the simulations, we observed the creation of turbulent flames, the development of ignition centers, and the subsequent transition to detonation. These and related simulations are reviewed here and presented in more detail in many of the references [1–20] listed in Table 1. At the end of this paper, we summarize where we are now in our understanding of DDT and suggest future directions.

2. Can we compute DDT?

If we define DDT as a detonation occurring in the vicinity of a turbulent flame, the answer to this is *probably yes*.

Fig. 1 is a sequence of images taken from a computation of the evolution of a system containing a turbulent flame in an ethylene–air mixture [9]. The entire simulation, from which this relatively small part is extracted, is described in more detail later in this paper. Each frame is an instant in a very dynamic scenario typical in a high-speed, compressible, chemically reactive flow. There are shocks, shear layers, large and small vortices, and contact surfaces, all in the vicinity of a turbulent flame. The shock front (marked S in Fig. 1) consists of a number of intersecting shocks and is moving to the left at about Mach 2. As the system evolves from frame 1 to 4, the upper part of the shock (Mach stem) becomes stronger.

Frame 3 shows that at some point, several locations in the unburned, turbulent material behind the Mach stem ignite spontaneously. Ignition centers develop into flames and produce shocks that ignite surrounding hot material and merge into an overdriven detonation front (frame 4). The detonation quickly spreads beyond the Mach stem and decays as it propagates (frames 5–8). Transverse-wave structure, typical of propagating detonations, is visible as "lines" extending behind the detonation front in frames 7 and 8. As the overdriven detonation de-

---

[1] This commonly refers to the statement that computer power available increases exponentially. For the past 20 years, it has doubled roughly every 18 months.

Table 1
Computations performed

Material/set	Dimension	Refs.	Comments
Acetylene–air 1. Shock–flame interaction	2D, 3D	[1,2]	Isolated effects of Richtmyer–Meshkov interactions on flame structure
Acetylene–air Shock–flame interactions and DDT 2. No boundary-layer effects	1D, 2D	[2–7]	Low-pressure system, 6-spark experiments Systematically examined effects of shock strength Related results to experiments and other approaches to studying DDT
3. No boundary-layer effects	2D		Varied location, shape of flame, Le Preliminary results, work unfinished
4. Boundary effects included	2D	[8]	Computation not resolved, but suggestive Raised fundamental issues about the effects of boundaries, turbulence
Ethylene–air Shock–flame interactions and DDT 5. Flame, boundary layer	2D, 3D	[9–12]	Low-pressure system, 1-spark experiments Boundary layer interacts with reflected shock to produce bifurcated shock Vortex behind bifurcation acts as a flame holder, creates supersonic flame
Ethylene–air Shock-induced ignition 6. Shock, boundary layer	2D	[8,13,14]	Reflected-shock, boundary layer Varied incident shock strength Autoignition in vortices caused by interactions of shock and boundary layer
Ethylene–air Shock–flame interactions and DDT 7. Flame, obstacle	2D	[11,15]	Low-pressure system, 1-spark experiments Similarities noted between effects of wakes behind obstacles and boundary layers
Hydrogen–air 8. Flame acceleration and DDT in channels with obstacles	2D, 3D	[16]	
^{12}C–^{16}O Propagation of turbulent flames and detonations in a white dwarf star	3D		Thermonuclear reactions Rayleigh–Taylor instability
9. White dwarf explosion leads to Type Ia supernova		[17–20]	Computations indicate DDT required to reconcile observations and theory Not completed; problems with disparity of physical scales

cays to the Chapman–Jouguet (CJ) state, these very closely spaced transverse waves decrease in number and spread out more along the front.

Fig. 2 has been extracted from a different computation of DDT in an acetylene–air mixture [8]. Here the colors are reversed from those in the previous picture: the blue material is burned, and the red or pink is unburned. The turbulent flame surfaces burn into the unreacted region, generating a complicated series of pressure waves and weak shocks. Hot spots form in the unreacted material and ignite at several locations and at different times. Eventually, one of these hot spots produces a detonation.

Finally, consider a fragment of another computation of the formation of a detonation in a confined acetylene–air mixture. Fig. 3 consists of a sequence of density, energy-release-rate, and pressure maps extracted from a much larger computation of a detonation arising from a shock–flame interaction [3]. This figure focuses on a funnel of unburned material surrounded by burned material. The top boundary of each frame is a symmetry plane. The bottom and side boundaries extend into a much larger computational domain. Note that the frames are not evenly spaced in time and that the time differences become much smaller starting at 865.9 µs.

At the earliest time (bottom frame of each column), 857.6 µs, there are two shocks (red regions on density maps) moving from right to left through the unreacted material. The first ignition that occurs, at 859.0 µs behind the shock on the right side, produces another shock and leaves a flame behind it. The second ignition behind the same shock, at 866.1 µs, produces a detonation. Once the detonation is ignited, it propagates through the funnel of unburned mater-

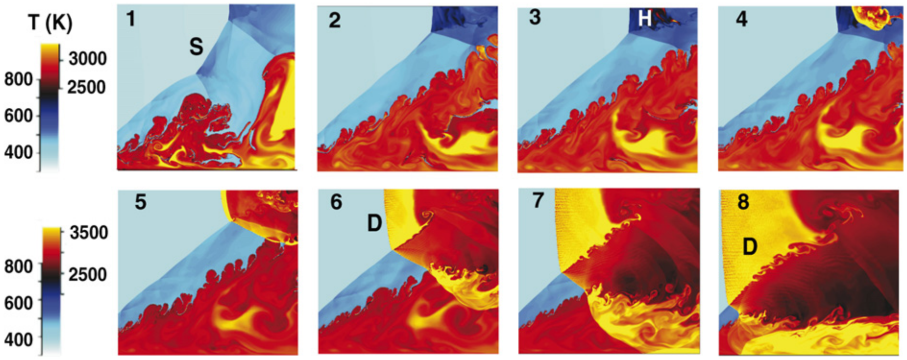

Fig. 1. Sequence of frames showing temperature distributions in a complex flow that leads to a detonation. Frames are extracted from a computation that tracks the evolution of a series of shock–flame interactions in an ethylene–air mixture [9,11]. Each frame is 4.2 × 3.8 cm. Boundaries: Bottom is a slip wall where a boundary layer develops; top is a symmetry plane; left and right extend into a much large computational domain (discussed later in text). Note that the color scales (left of images) are double-valued, with the left scale for unreacted material and the right scale for burned material. Detonation ignition occurs in spots next to the H on frame 3. S: shock wave, moving from right to left; H: hot spot or ignition center; D: detonation wave showing transverse wave structure. Frame 1: 437 µs; Frame 2: 485 µs; Frame 3: 496 µs; Frame 4: 503 µs; Frame 5: 507 µs; Frame 6: 515 µs; Frame 7: 524 µs; Frame 8: 533 µs.

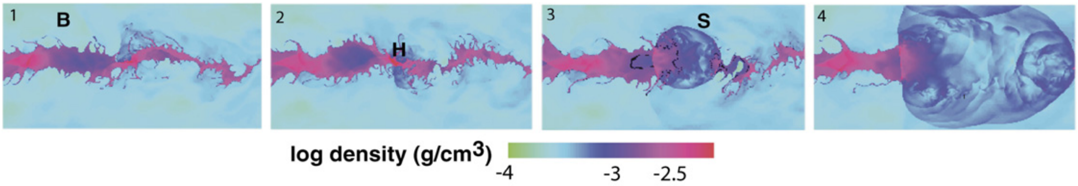

Fig. 2. Sequence of frames showing density distribution, extracted from a larger computation of detonation ignition in a sinuous funnel of unburned material surrounded by a turbulent acetylene–air flame [8]. Each frame is 2 × 1 cm. Top and bottom boundaries are slip walls, left and right extend into a much larger computational domain. Blue regions are burned (marked B), pink regions are unreacted material (marked U). The explosion of a hot spot (near the H) occurs near the center of the funnel in frame 2. This leads to a shock (S) and a detonation (D). Frame 1: 765 µs; Frame 2: 770 µs; Frame 3: 775 µs; Frame 4: 780 µs.

ial and consumes any unreacted material left in the chamber.

There are notable similarities and differences among the calculations shown in Figs. 1–3. In all cases, the detonation developed from a hot spot igniting in unreacted material. Sometimes the hot spots did not become detonations, but resulted in decoupled shocks and flames. One interesting point is that it was not the flame that underwent transition to a detonation, but the detonation arose in unreacted material in the vicinity of the flame. Is this DDT? The remainder of this paper includes more detailed descriptions of these phenomena and an attempt to understand what DDT is and when it occurs.

3. Background

This section is *not* intended as a complete review of our current understanding of DDT. Instead, it presents the background theoretical and experimental information needed to understand the results discussed in the rest of the paper. For historical background, it is interesting to read the early descriptions of experiments on DDT given by Brinkley and Lewis [21], who based their interpretation on the turbulent flame theory proposed by Karlovitz [22]. Later experimental work by Oppenheim and coworkers [23–25] went a long way toward observing DDT in shock-tube experiments. Useful summaries of mechanisms of DDT have been given by Lewis and von Elbe [26] and Kuo [27]. Excellent, more recent reviews have been written on DDT by Lee [28], Shepherd and Lee [29], and Lee and Moen [30].

3.1. Experimental studies of DDT

As described in the Introduction, there are several ways DDT has been studied experimentally. One is by igniting a flame using a spark at one end of a long channel containing an energetic gas. For exam-

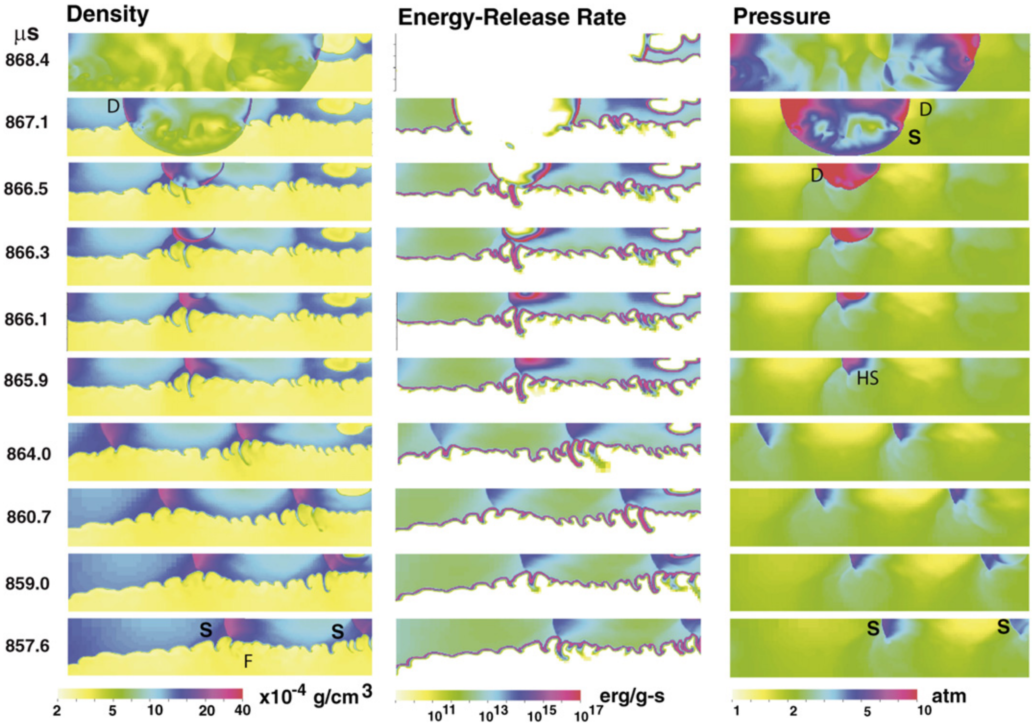

Fig. 3. DDT inside a small funnel of unburned material surrounded by a flame [3], as shown by density, energy-release rate, and pressure at selected times. Frames 0.5 × 0.1 cm extracted from a much larger computation. Top of domain is a symmetry plane; bottom, left, and right extend into a much large computational domain. Flow is generally moving from right to left. In each frame, unreacted material is on the top and burned material on the bottom. Physical time is shown in μs on the left side. S: shock fronts; F: flame; D: detonation; HS: hot spot.

ple, Urtiew and Oppenheim [23] carried out a series of experiments in long, enclosed channels containing hydrogen and oxygen. They ignited the mixtures at one end of the tube, creating an initially laminar flame that accelerated, became turbulent, and produced a detonation. When DDT occurred, it appeared to be a sudden explosion in the vicinity of this flame. Two basic scenarios of DDT were observed: sometimes it happened inside the region containing the turbulent flame, and sometimes it occurred in the preheated, compressed material between the leading shock wave and the flame. A substantial body of experimental work has since shown that the presence of obstacles along the walls of the channels results in much faster flame acceleration and transition to a detonation than if no obstacles were present (see, for example, [29–34]).

A second type of experiments, based on the work of Markstein [35], used a shock–flame interaction to create the turbulent flame more quickly [36–39]. A flame was ignited by sparks at a distance from a reflecting wall, and then a shock was released at the opposite end of the tube. The flame interacted first with the incident shock and later with the shock reflected from the end wall. Shock–flame interactions distorted the flame, making it turbulent and increasing the energy-release rate in the system. These experiments showed a number of specific DDT-related phenomena and well-defined trends on which simulations could be focused. For example, whether and where DDT occurred in the system depended on the Mach number of the incident shock. For the lowest Mach numbers, the reflected shock was amplified by the turbulent flame, but there was no DDT. For intermediate Mach numbers, DDT occurred between the flame brush and the reflected shock. For the highest Mach numbers DDT occurred inside the flame brush. Whenever DDT occurred, the transition was through a very rapid explosion whose details could not be determined from the experiment.

Experiments in which DDT arises after a shock–flame interaction and the creation of a turbulent flame are particularly well suited for numerical modeling because the flow develops relatively quickly. Markstein's experiments showed that the first and major effect of the interaction of a curved flame and a shock is a large funnel of unburned material that extends into the burned region [35]. The funnel forms as a result of the Richtmyer–Meshkov (RM) instability [40, 41], which develops as a shock impulsively accelerates a perturbed contact discontinuity. In this case, the contact discontinuity is a flame surface. The RM interaction distorts the flame surface on smaller scales when incident or reflected shocks cross the perturbed flame surface from any direction. This provides an important mechanism for turbulence generation and drastically accelerates the development of a turbulent flame that may eventually create conditions for detonation initiation.

Finally, experiments attempting to observe unconfined DDT [42–44] showed that a transition to detonation induced by turbulent flames in systems without walls or obstacles is rather difficult. This can be partially attributed to the lack of shock-reflecting surfaces. It can also be partially due to geometrical effects of expansion: shocks proceeding from a deflagration might be weakened, or turbulence might be damped too much by the expansion, and so they become unable to precondition the gas for DDT. Wagner [42] reports experiments in which deflagrations were forced to DDT by passing through screens of specified mesh sizes. The screens created turbulence of the required scale and intensity. These experiments suggest that an unconfined deflagration could make the transition to detonation under the right conditions.

A related problem that was studied experimentally is initiation of detonations by turbulent jets [43,45–48]. In these experiments, a jet of hot combustion products was injected into an unburned, cold mixture. The turbulence created by the interaction of this jet and the background gas created a nonuniform, preconditioned region in which detonation could occur. These experiments provide important information on the critical size of the region capable of triggering DDT when the effects of reflected shocks and interactions with walls are minimal.

The most extreme case of unconfined DDT is an initially laminar flame inside a very large volume of a reactive mixture with no preexisting turbulence or shocks. In the absence of effective mechanisms for turbulence generation, such as shock–flame interactions and wakes, laminar flames become turbulent through other, relatively slow mechanisms, such as Darrieus–Landau and thermal-diffusive instabilities. In the presence of gravity, the buoyancy-driven Rayleigh–Taylor (RT) instability might become a dominant mechanism for turbulence generation. The developing turbulence, however, might be damped by expansion. The size of unconfined systems in which DDT could be observed is expected to be relatively large. It has been suggested, for example, that DDT might occur in very large vapor clouds [30,49].

Analysis of experimental data shows that turbulence plays an important role in DDT. Several apparently different mechanisms for DDT have been described, each including the effects of turbulence and formation of shocks. On large scales, turbulence deforms the flame front and increases its surface area. On small scales, it can broaden the flame front and cause mixing. The result is an extended turbulent "flame brush" in (or near) which a series of explosions occurs. One of these explosions finally leads to a detonation. Other routes to detonation may include an explosion in the boundary layer, or an explosion in the region between the leading shock and flame brush.

This summary of observational evidence does not address the intrinsic mechanism by which a detonation appears. It does, however, give us a general picture of when and where DDT might occur and the importance of fluid instabilities in creating the turbulent background in which DDT is more likely to appear. At this point in this discussion, the relation between the physical mechanisms responsible for DDT in these experiments is not entirely clear, and the events leading to DDT seem to vary with the particular scenario in which it is observed.

3.2. Theoretical and numerical studies

The basis for interpreting the simulations described in this paper was formed by many previous theoretical and numerical studies of DDT that focused on different parts of the problem. Hot spots that could lead to DDT were analyzed by Merzhanov [50] and Borisov [51]. A hydrodynamic model of a hot spot acting as an expanding piston was studied by Zajac and Oppenheim [52]. Meyer and Oppenheim [53] suggested that the variation of the induction time among many hot spots must be small in order for a detonation to appear.

The question of how exactly a hot spot can give rise to a detonation remained open until Zeldovich et al. [54] proposed the idea of the ignition of a detonation in a gradient of reactivity. A similar concept of shock-wave amplification by coherent energy release (SWACER) was introduced by Lee et al. [55]. The basic idea is that a *spontaneous reaction wave* can propagate through a reactive material if there is a spatial gradient in chemical induction time τ_c. The wave appears when the material spontaneously ignites at the location of the minimum τ_c and spreads by spontaneous ignition at neighboring locations where τ_c is slightly longer. The resulting spontaneous wave is analogous to a phase wave and propagates in the direction x with the velocity $D_{sp} = (\partial\tau_c/\partial x)^{-1}$, which cannot be lower than the laminar flame speed, but is not limited from above and can even exceed the speed of light. (See [56–59] for discussion of D_{sp} and different regimes of reaction front propagation.) When D_{sp} falls in the interval roughly limited by the speed of sound and the Chapman–Jouguet detonation velocity D_{CJ}, the spontaneous reaction wave and the compression wave generated by the exothermic reaction can couple and evolve into a self-sustained detonation wave. The SWACER mechanism suggests that this evolution occurs through the amplification of shock waves propagating through the gradient of reactivity with a velocity close to D_{sp}. The gradient concept proposed by Zeldovich et al. is more general and also allows the detonation to form when a spontaneous wave decelerates from higher velocities to D_{CJ} (see [58] for more details). Now there is substantial experimental and theoretical evidence that a detonation can develop in a reactivity gradient [30,32,54,55,57,58,60–62]. Nevertheless, the relation of this mechanism to detonation ignition in a turbulent flame brush was not at all certain when we began this project.

Numerical investigations of the RM instability were first reported by Youngs [63]. In these calculations, a shock interacted with a curved density discontinuity. Much of the subsequent work investigated how the RM instability affects the laser–pellet interaction found in inertial confinement fusion and how to suppress or enhance it (see, for example, [64]). A detailed numerical study of RM instability in two and three dimensions, including a comparison with the nonlinear theory, has been performed by Li and Zhang [65]. A general review on RM instability was recently published by Brouillette [66]. A number of experiments (e.g., [67,68]) and simulations (e.g., [69–71]) considered the related problems of shock–bubble or shock–droplet interactions.

The first attempts to model the effects of a flame–shock interaction were by Picone et al. [72]. The flame was modeled as a hot bubble and the flame surface as a nonreacting discontinuity between hot burned material and cold background material. This work assumed that the energy release was negligible on the timescales of the shock–flame interaction and focused on the vorticity generated by the flame–shock interaction itself. A similar computation with a full chemical reaction mechanism compared the effects of mixing with and without chemical reactions [73]. Again, emphasis was on the vortex structure and how this was affected by energy release. The vorticity field generated by a single planar pressure wave moving through a cylindrical laminar flame was also examined in [74]. The shock–flame interaction creates vortices, and there has been significant work in flame–vortex–acoustic interactions (for a review, see [75]; for more recent work, see, for example, [76]).

4. Physical and chemical models

The DDT simulations that produced Figs. 1–3 and most of the others discussed later in this paper solved the multidimensional, time-dependent, compressible reactive Navier–Stokes equations, which include models for compressible fluid convection, chemical reactions and energy release, molecular diffusion, thermal conduction, and viscosity,

$$\frac{\partial \rho}{\partial t} + \nabla \cdot (\rho \mathbf{U}) = 0, \tag{1}$$

$$\frac{\partial (\rho \mathbf{U})}{\partial t} + \nabla \cdot (\rho \mathbf{U}\mathbf{U}) + \nabla P + \nabla \cdot \hat{\boldsymbol{\tau}} = 0, \tag{2}$$

$$\frac{\partial E}{\partial t} + \nabla \cdot \big((E+P)\mathbf{U}\big) + \nabla \cdot (\mathbf{U} \cdot \hat{\boldsymbol{\tau}}) + \nabla \cdot (K \nabla T) + \rho q \dot{w} = 0, \tag{3}$$

$$\frac{\partial (\rho Y)}{\partial t} + \nabla \cdot (\rho Y \mathbf{U}) + \nabla \cdot (\rho D \nabla Y) - \rho \dot{w} = 0, \tag{4}$$

where ρ is the mass density, $\mathbf{U}$ is the velocity, E is the energy density, P is the pressure, Y is the mass fraction of a reactant, $\dot{w} = \mathrm{d}Y/\mathrm{d}t$ is the reaction rate, q is the total chemical energy release, K is the thermal conduction coefficient, D is the mass diffusion coefficient, and

$$\hat{\boldsymbol{\tau}} = \rho \nu \left(\frac{2}{3} (\nabla \cdot \mathbf{U}) \mathbf{I} - (\nabla \mathbf{U}) - (\nabla \mathbf{U})^{\dagger} \right) \tag{5}$$

is the viscous stress tensor which includes terms arising in compressible Navier–Stokes equations with zero bulk viscosity. Here ν is the kinematic shear viscosity, $\mathbf{I}$ is a unit matrix, and superscript $\dagger$ indicates matrix transposition. The equation of state is that of an ideal gas,

$$P = \frac{\rho R T}{M}, \qquad \epsilon = \frac{P}{(\gamma - 1)}, \tag{6}$$

where $\epsilon = E - \rho U^2/2$ is the internal energy density, γ is the adiabatic index, R is the universal gas constant, and M is the molecular weight.

Because we are doing multidimensional combustion simulations over length scales of meters and deal with reaction scales on the order of millimeters and less, we need chemical and thermophysical models that reproduce the major features of the system and yet are practical computationally. In this study, we used a one-step reaction model described by the first-order Arrhenius kinetics,

$$\frac{\mathrm{d}Y}{\mathrm{d}t} \equiv \dot{w} = -A \rho Y e^{-Q/RT}, \tag{7}$$

where A is the preexponential factor and Q is the activation energy. The reaction rate $\dot{w}$ is proportional to ρ to account for the binary nature of chemical reactions taking place in typical combustion systems.

We assume that kinematic viscosity, diffusion, and heat conduction have a similar temperature dependence,

$$\nu = \nu_0 \frac{T^n}{\rho}, \qquad D = D_0 \frac{T^n}{\rho}, \qquad \frac{K}{\rho C_{\mathrm{p}}} = \kappa_0 \frac{T^n}{\rho}, \tag{8}$$

Table 2
Material, chemical, and reaction-wave parameters for acetylene–air

Quantity	Value	Definition
	Input	
T_0	293 K	Initial temperature
P_0	1.33×10^4 J/m^3	Initial pressure
ρ_0	1.58×10^{-1} kg/m^3	Initial density
Y_0	1	Initial composition
γ	1.25	Adiabatic index
M_s	29	Molecular weight
A	1×10^9 m^3/kg/s	Preexponential factor
Q	$29.3RT_0$	Activation energy
q	$35.0RT_0/M$	Chemical energy release
$\nu_0 = \mu_0 = D_0$	1.3×10^{-6} (g/s cm K$^{0.7}$)	Transport constants
	Output	
T_b	2340 K	Adiabatic flame temperature
ρ_b	1.98×10^{-2} kg/m^3	Adiabatic flame density
S_l	$\simeq$1.44 m/s	Laminar flame speed
x_l	$\simeq$0.25 mm	Laminar flame thickness
T_s	1500 K	Postshock detonation temperature
ρ_s	1.15 kg/m^3	Postshock detonation density
D_{CJ}	1870 m/s	Chapman–Jouguet detonation velocity
x_d	$\simeq$0.5 mm	One-dimensional detonation thickness

where ν_0, D_0, and κ_0 are constants, $C_p = \gamma R/M(\gamma - 1)$ is the specific heat at constant pressure, and $n = 0.7$ emulates a typical temperature dependence of these coefficients in reactive hydrocarbon systems. The nondimensional Lewis, Prandtl, and Schmidt numbers, independent of thermodynamic conditions, can be expressed as

$$\mathrm{Le} = \frac{K}{\rho C_p D} = \frac{\kappa_0}{D_0}, \qquad \mathrm{Pr} = \frac{\rho C_p \nu}{K} = \frac{\nu_0}{\kappa_0},$$
$$\mathrm{Sc} = \frac{\nu}{D} = \frac{\nu_0}{D_0}. \tag{9}$$

Given Eqs. (1)–(9), we require input values for the chemical and thermophysical parameters for a particular energetic gas that are close to those experimentally defined and, when used in test computations, produce ignition, flame, and detonation properties that are reasonably in line with those measured or computed from more detailed models. Finding such a consistent set of input parameters requires iterations and testing, and is a topic worthy of further study in itself. For example, given that the input variables are background conditions (temperature, pressure, and density), chemical energy release, preexponential factor, activation energy, and diffusive transport coefficients, the model should be able to reproduce induction delays, a one-dimensional flame with the correct flame thickness, laminar flame velocity, and adiabatic flame temperature, a one-dimensional detonation with the correct thickness, CJ velocity, and postshock temperature and reasonable two-dimensional detonation cell sizes. Sets of these parameters were derived for the stoichiometric, low-pressure acetylene–air (Table 2) and ethylene–air (Table 3) mixtures used in the first experiments we modeled.

4.1. Models for acetylene–air and ethylene–air

There are neither direct experimental data on induction delays nor reliable detailed chemical reaction models for the acetylene–air mixture used in the shock-tube experiments, although there are relevant data for closely related systems. The model parameters were selected to be "reasonably" physical and, when used in computations, reproduced the laminar flame speed S_l, laminar flame thickness x_l, detonation wave speed D_{CJ}, and detonation wave thickness in acetylene–air in the pressure range from 0.1 to 1 atm for a system initially at room temperature.

The value of the energy release q was selected to give the correct value of D_{CJ}. The value of the activation energy Q in Eq. (7) was based on experiments by Glass et al. [77], who determined Q for $C_2H_2 + O_2 + Kr(Ne)$ at temperatures of 1200–2200 K and found that it was somewhat insensitive to the amount of diluent. The experimentally determined chemical induction time of $C_2H_2 + O_2 + Kr(Ne)$ is assumed to be a reasonable estimate of that for $C_2H_2 + O_2 + N_2$ (Wing Tsang, personal communication).

The transport coefficients, comparable to these of air under the same conditions, and the preexponential factor A were selected to reproduce x_l (Geraint Thomas, personal communication) and to make the

Table 3
Material, chemical, and reaction-wave parameters for ethylene–air

Quantity	Value	Definition
	Input	
T_0	293 K	Initial temperature
P_0	$1.33 \times 10^4\ \mathrm{J/m^3}$	Initial pressure
ρ_0	$1.58 \times 10^{-1}\ \mathrm{kg/m^3}$	Initial density
Y_0	1	Initial composition
γ	1.15	Adiabatic index
M_s	29	Molecular weight
A	$3.2 \times 10^{11}\ \mathrm{m^3/kg\,s}$	Preexponential factor
Q	$30.74RT_0$	Activation energy
q	$61.03RT_0/M$	Chemical energy release
$\nu_0 = \mu_0 = D_0$	$7.0 \times 10^{-6}(\mathrm{g/s\,cm\,K^{0.7}})$	Transport constants
	Output	
T_b	2625 K	Adiabatic flame temperature
ρ_b	$1.77 \times 10^{-2}\ \mathrm{kg/m^3}$	Adiabatic flame density
S_l	$\simeq$1.28 m/s	Laminar flame speed
x_l	$\simeq$0.96 mm	Laminar flame thickness
T_s	1081 K	Postshock temperature
ρ_s	$1.66\ \mathrm{kg/m^3}$	Postshock density
D_{CJ}	1870 m/s	CJ detonation velocity
x_d	$\simeq$1.46 cm	One-dimensional detonation thickness

one-dimensional detonation wave thickness x_d consistent with the detonation wave spacing data [79]. We assumed that x_d is roughly $1/20$–$1/50$ of the detonation cell size, and $Le = Sc = Pr = 1$. This physical model gives the correct pressure dependence of x_l and S_l [78] and the detonation cell size [79]. Induction times are comparable to those in the experiments [77].

The adiabatic index was assumed to be constant, $\gamma = 1.25$, and independent of composition. The value chosen is consistent with the low values predicted by the Gordon–McBride code [80] for acetylene–air in the range of temperatures and pressures of interest. In a model with constant γ, it is not generally possible to fit D_{CJ} and the adiabatic flame temperature T_{ad} independently. We found that T_{ad} in the model is close to that computed by the Gordon–McBride code, although it is slightly higher (by approximately 200 K). We decided to fit D_{CJ} exactly and let T_{ad} be overestimated. This does not affect the computed flame speed and thickness, and thus, the rate of energy release by the flame is correctly described.

The input for the ethylene–air model was constructed in a similar way and is summarized in Table 3. In this case, the value of $\gamma = 1.15$ is also consistent with the values predicted by the Gordon–McBride code for ethylene–air. The value of Q, the activation energy, is based on experiments by Glass et al. [77] and was used by Strehlow and Engel [79] in their detonation studies.

5. Numerical models and issues

Solving reactive Navier–Stokes equations requires making a series of decisions, such as selecting numerical algorithms and the complexity of the submodels representing various physical and chemical processes [81]. The accuracy of the solution is also bounded by available computational resources and, as discussed in the Introduction, the length of our lives. The 1996 timing estimates described in the Introduction were based on using simplified representations of the chemical reactions and diffusive transport processes discussed in the previous section and a standard high-order algorithm to solve Eqs. (1)–(9) on a static, uniform grid. We considered a shock tube about 1 m long containing a low-pressure acetylene–air mixture, defined in Table 2, and assumed that computations should resolve the laminar flame thickness, x_l.

The 1996 timing estimates proved to be, in turn, both daunting and provocative. They did inspire the invention and development of a series of numerical tools and algorithms, including methods for integrating sets of nonlinear stiff ordinary differential equations (ODEs), methods for adaptive mesh refinement (AMR), and techniques for parallelizing programs on a variety of computer architectures. Many of these methods and techniques are described in [81]. Those that were critical for studies of the DDT problem are discussed here and in [1–20].

5.1. Adaptive mesh refinement: The fully threaded tree

The general solution method for Eqs. (1)–(9) usually proceeds by dividing physical space into computational cells, discretizing these partial differential equations in space and time, and then solving the discretized set of algebraic equations. The problems in which we are interested involve some system-sized and some nearly microscopic spatial regions of intense activity and other regions where very little appears to be happening. As the solution of the problem evolves, these regions are continually changing: they move, grow, and shrink, and new ones appear and disappear. To handle important changes in the flow or reactivity and to resolve the very disparate space scales involved in DDT, we needed a reliable, responsive method for locally refining and coarsening the computational mesh.

Such a method was developed by Khokhlov [82]. This method uses an adaptive grid with the data structure based on the fully threaded tree (FTT). In computer memory, computational cells are organized onto an oct-tree structure (in three dimensions, each cell can be divided into eight cells). The entire computational domain is represented by the root cell of the tree. The root has smaller cells, its children, which may have their own children, etc. The tree grows dynamically when the cells are refined, and it shrinks when the cells are coarsened. Any cell can be refined or coarsened independently, and this gives maximal flexibility to the adapting algorithm. In physical space, square or cubic cells of different levels are organized in a structured Cartesian mesh, where neighboring cell sizes can be the same or differ by a factor of 2.

Each FTT cell contains information about the physical state in the cell and a number of pointers to the cell's children, parents, and neighbors. The threading pointers provide the grid connectivity information that eliminates the need for a tree search and allows parallel operations on the FTT, including mesh modifications. A parallel FTT suitable for the DDT calculations is now implemented as a library of subroutine calls, and it is operational on distributed- and shared-memory parallel computers.

5.2. Solutions of Navier–Stokes equations

The fluid-dynamics equations were solved using an explicit, second-order, Godunov-type numerical scheme implemented on the FTT-based adaptive mesh [82]. Because of restrictions in the way the operative version of the FTT was parallelized, we used a relatively low-order method to solve the fluid-dynamic equations. This means that the algorithm is more diffusive than algorithms we commonly use, but we hoped to compensate for this with the locally high resolution allowed by the FTT. Current algorithmic advances include extending the fluid solver to a higher-order flux-corrected transport method [83]. This should give us higher accuracy and better control of subgrid dissipative effects for turbulent flows, as well as allowing a more general implementation of the FTT.

5.3. Numerical resolution

The only way to test if a complicated numerical simulation is a good solution of the equations is by performing resolution tests [81]. This means varying sizes of computational cells and time steps to the point where the solutions no longer change. We then say that the solution is "converged." This is a different question from whether we are solving the correct set of equations, whether these equations represent the physical system we want them to, or whether we are actually translating the equations into the best forms for numerical solution. Nonetheless, convergence is a critical test of the validity of the computation.

There are several aspects of and issues related to resolution tests that have to be noted. First, it is possible for different properties of a flow to become resolved at different computational cell sizes. Second, different amounts of resolution might be acceptable for different problems or different aspects of the same problem. And finally, convergence itself could be affected by the specific numerical algorithms used. These sorts of issues are usually treated in standard text books on computational fluid dynamics. They are more difficult in reactive flow simulations and in other types of simulations that contain many disparate time scales. In a problem such as DDT, it is easy to imagine never finding the hot spot and still seeing major features of the solution resolved, or finding different hot spots at different resolutions. Resolution tests will show if the one found is really a property of the set of equations.

Because of the novelty of some of the results presented below, resolution tests were the only way to convince ourselves that phenomena observed in the calculations were correct solutions of the equations. As such, they are referred to often in this paper. At the present time, rigorous resolution tests are usually too expensive to perform for three-dimensional simulations. In these cases, we can only use what we have learned from the two dimensions and "do the best we can."

6. Interactions of shocks, flames, and boundary layers

Table 1 summarizes major sets of simulations performed at NRL to study DDT arising from a turbu-

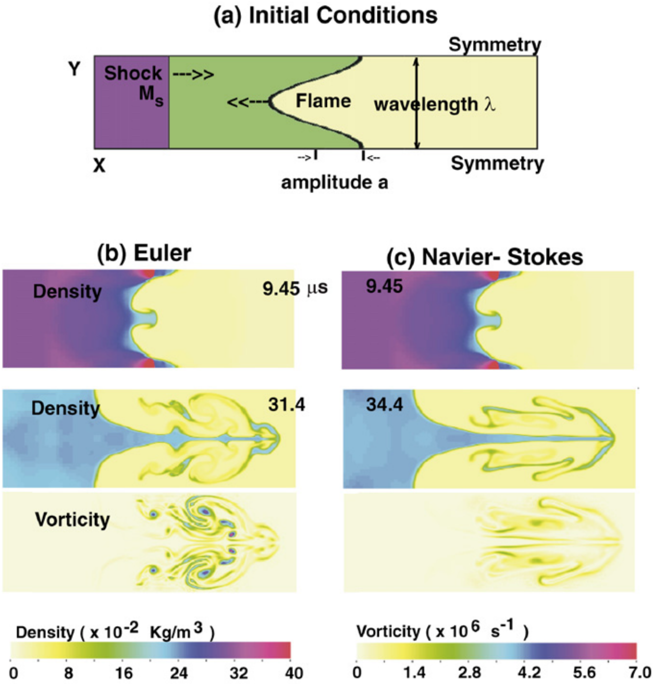

Fig. 4. (a) Schematic of initial conditions for two-dimensional planar shock–flame interaction computation in acetylene–air at 293 K and 100 Torr [1]. Incident shock strength $M_S = 1.5$, flame thickness $x_l = 0.25$ mm, perturbation wavelength $\lambda = 0.25$ cm, perturbation amplitude $a = 0.125$ cm. (Details of the initial set up and the time-dependent left and right boundary conditions are given in [1].) (b) Nonreactive Euler computations. Density distributions shown at 9.45 and 31.4 µs; vorticity distribution shown at 31.4 µs. (c) Nonreactive Navier–Stokes computation of shock–flame interaction. Density distributions shown at 9.45 and 34.4 µs; vorticity distribution shown at 34.4 µs. Each frame in (b) and (c) is 0.91 cm long and 0.25 cm high.

lent flame created by multiple shock–flame interactions. These computations solved Eqs. (1)–(9), used the same or very similar numerical algorithms, and modeled laboratory-scale experiments. The exception is the last set of computations that modeled Type Ia supernova explosions involving thermonuclear turbulent flames dominated by Rayleigh–Taylor instabilities.

6.1. A shock–flame interaction

Set 1 in Table 1 isolated two aspects of the DDT problem: a flame propagation in a channel and the interaction of a single shock with a curved flame or density discontinuity [1]. The calculations in [1] did not directly address the DDT problem, but were used to benchmark the code and give insights into the nonlinear evolution of fluid and combustion instabilities. A schematic of the computational domain is shown in Fig. 4a. A shock was placed near the left boundary, and conditions to the left of the shock were set as a uniform flow with postshock parameters determined from the Rankine–Hugoniot conditions for a shock with Mach number M_S. The left boundary provides a constant inflow of gas until rarefactions and sound waves from the shock–flame interaction reach that boundary. Then the inflow is modified by outgoing waves. Ahead of the shock, the velocity of the gas is initially set to zero. The initial discontinuity was not planar, but characterized by a wavelength (usually controlled by changing the height of the channel) and wave amplitude. The initial conditions in the low-density region to the right of the discontinuity are those that we would expect behind an acetylene–air flame. To increase the time for which we can follow the flame evolution, the computations were performed in a coordinate system moving with some constant velocity relative to the laboratory system. This was done by subtracting a constant relative velocity everywhere from the initial conditions at the beginning of the simulations. (Further description of the computational setup is given in [1].)

The major effect of a planar shock interacting with a curved density discontinuity is to invert the surface, driving the part of the initially concave surface inwards behind the shock. The result is that a “funnel” or “spike” of heavy material extends into the region of light material. This funnel is topped off with a mushroom-shaped cap. Two large vortices develop near the cap, and soon secondary instabili-

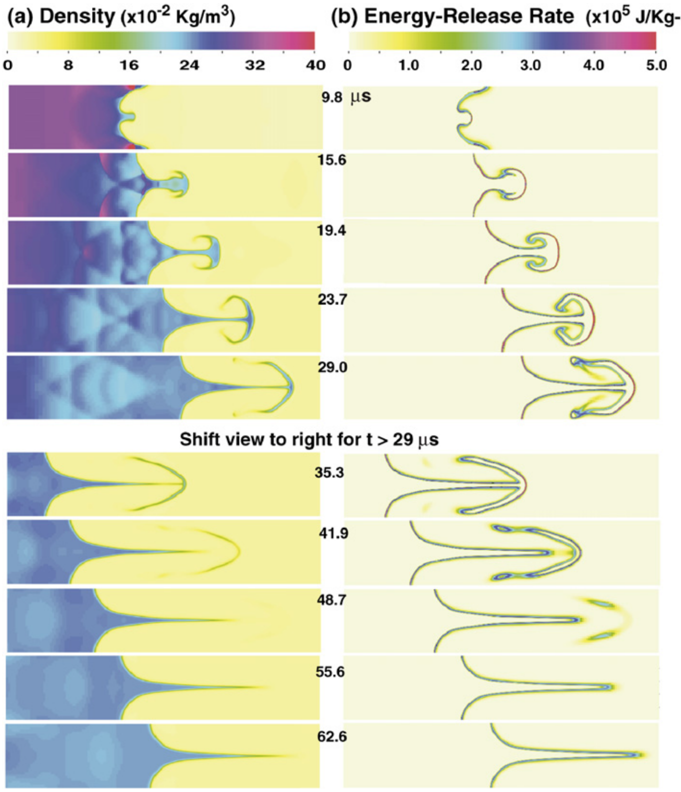

Fig. 5. (a) Density (left column) and (b) energy-release rate (right column) for a typical computation of a shock–flame interaction [1]. Each frame is 1.25 cm long and 0.25 cm high. Times (in µs) are given in the center between the density and energy release. Note that the frames after 29 µs are shifted to the right by the same amount in order to show the extent of the interaction.

ties form along the perturbed discontinuity. Figs. 4b and 4c compare two-dimensional planar nonreactive Navier–Stokes and Euler simulations of a $M_S = 1.5$ shock interacting with a density discontinuity. In both the Navier–Stokes and Euler cases, the main features grow at essentially the same rate. In the Navier–Stokes case, however, the growth of secondary instabilities along the funnel is suppressed.

The interaction of the same strength $M_S = 1.5$ shock and a curved flame is summarized in the time sequence of frames shown in Fig. 5. Again, the perturbed surface becomes inverted and the funnel grows, in a way similar to that shown for the nonreactive cases. Now, however, the small-scale features due to the secondary instabilities are absent because they burn out. Both the funnel and the mushroom become thinner as the burning proceeds. Eventually, the mushroom cap separates from the funnel and disappears, leaving just a spike. At later times that are not shown here, the vorticity decays and the spike evolves into the typical Landau–Darrieus shaped flame. Figs. 4 and 5 are results from selected two-dimensional calculations, which were part of an extensive series of two- and three-dimensional Euler and Navier–Stokes, reactive and nonreactive computations in which the wavelength and amplitude of the perturbation were varied and the results tabulated and compared [1]. For future discussion of the DDT, it is important to note that the increase in the energy-generation rate due to a *single* shock–flame interaction is about a factor of 20 or 30, and occurs over a very short time period. In itself, a single shock–flame interaction did not lead to a detonation.

6.2. Multiple shock–flame interactions and DDT

Set 2 in Table 1 was based on experiments in which simultaneous, vertically aligned sparks ignited flames in a channel filled with an acetylene–air mixture [2–5,7]. Fig. 6 is a schematic that shows how the computational domain is embedded in the experiment and indicates the boundary conditions. We modeled a (32 × 1)-cm section of tube using reflecting boundary conditions on the right, a zero-gradient inflow–outflow boundary on the left, and symmetry (mirror) conditions on the upper and lower boundaries. The computational domain contains half of a cylindrically

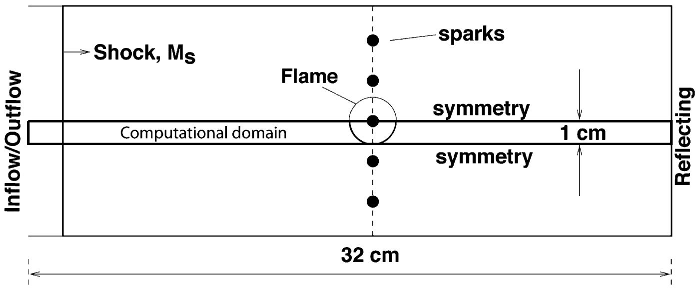

Fig. 6. Schematic of the experiment and computational setup for the multiple-spark shock–flame interaction in acetylene–air [2].

expanding flame produced by one of the sparks far from channel walls. A driven shock is initially placed 2 cm from the left boundary. The velocity of the gas is set to zero everywhere ahead of the shock. Between the left boundary and the shock, there is a uniform flow with the postshock parameters determined from the Rankine–Hugoniot conditions for a shock with a given Mach number, M_S. The left boundary condition provides a constant inflow of gas through this boundary until the rarefaction and sound waves from the eventual shock–flame interaction reach the boundary. Then the inflow is modified by outgoing waves. The initial flame has a radius of 1.5 cm and is centered 13 cm from the endwall. It is set up as a discontinuity separating the background region and a region with adiabatic flame conditions. After molecular diffusion and heat conduction spread the discontinuity, chemical reactions begin and a self-consistent flame develops.

Fig. 7 is the time sequence of density fields computed for incident-shock strength $M_S = 1.5$. The initial frame, step 0, shows the shock on the far left and the unperturbed flame approximately in the middle of the domain. As time passes, this incident shock I approaches the flame, and the shock–flame interaction begins around step 400. When I interacts with the left side of the flame, the result is a rarefaction wave that moves back upstream, and a transmitted shock that moves through the flame. When this transmitted incident shock interacts with the right side of the flame, it produces a weak reflected shock R1 that also moves upstream, first through the material burned by the flame, and then through the initially shocked, unburned material. The rarefaction wave and R1 can be seen in frames 600 through 1700. The incident shock transmitted through the flame moves downstream toward the end wall, as seen in frames 600 and 800, and reflects from the wall by step 900. This produces a strong reflected shock R2.

The interactions of I and R1 with the flame trigger a Richtmyer–Meshkov (RM) instability, which creates a large funnel of unburned material that penetrates the burned region. At frame 1000, R2 begins to interact with the distorted flame. This generates a new sequence of reflected and transmitted shocks and rarefactions which further distort the flame. The shock R2 passes through the flame by step 1200, and continues to move upstream. It finally merges with R1 between steps 1700 and 1800. When R2 passes through the left side of the flame at step 1200, it generates another reflected shock that moves to the right. This shock passes through the flame, reaches the end of the tube, and reflects from the endwall between steps 1300 and 1400, producing the R3. The shock R3 passes through the flame again, further distorting the flame, and finally emerging from the left side of the flame at step 1600. This third emerging shock R3 propagates in material that was shocked three times previously (incident shock plus two reflected shocks). It eventually merges with the combined reflected shock (R1–R2) between steps 1900 and 2000.

Between steps 2200 and 2260, two sudden explosions occur almost simultaneously in the material behind the merged reflected shock, R1–R2–R3. These explosions coalesce to form a detonation that spreads in all directions. As it moves to the right, it enters the flame between steps 2400 and 2500 and decays into a shock. Now let us look at selected details of the interaction more closely. These and other features are examined in much more detail in [2].

6.2.1. Creation of the turbulent flame

Fig. 8 shows the energy-release rate as a function of time for the two-dimensional system and for an equivalent one-dimensional system. Three different numerical resolutions showed essentially the same result for the time history of the global energy-release rate in the two-dimensional system [2]. The energy-release rate is significantly higher than in the one-dimensional system because of the instabilities that increase the flame surface area in two dimensions. We now follow the development of these instabilities using Figs. 7 and 8.

As the flame grew with no shock interactions, its surface became slightly perturbed as it expanded. These initial perturbations were barely visible at

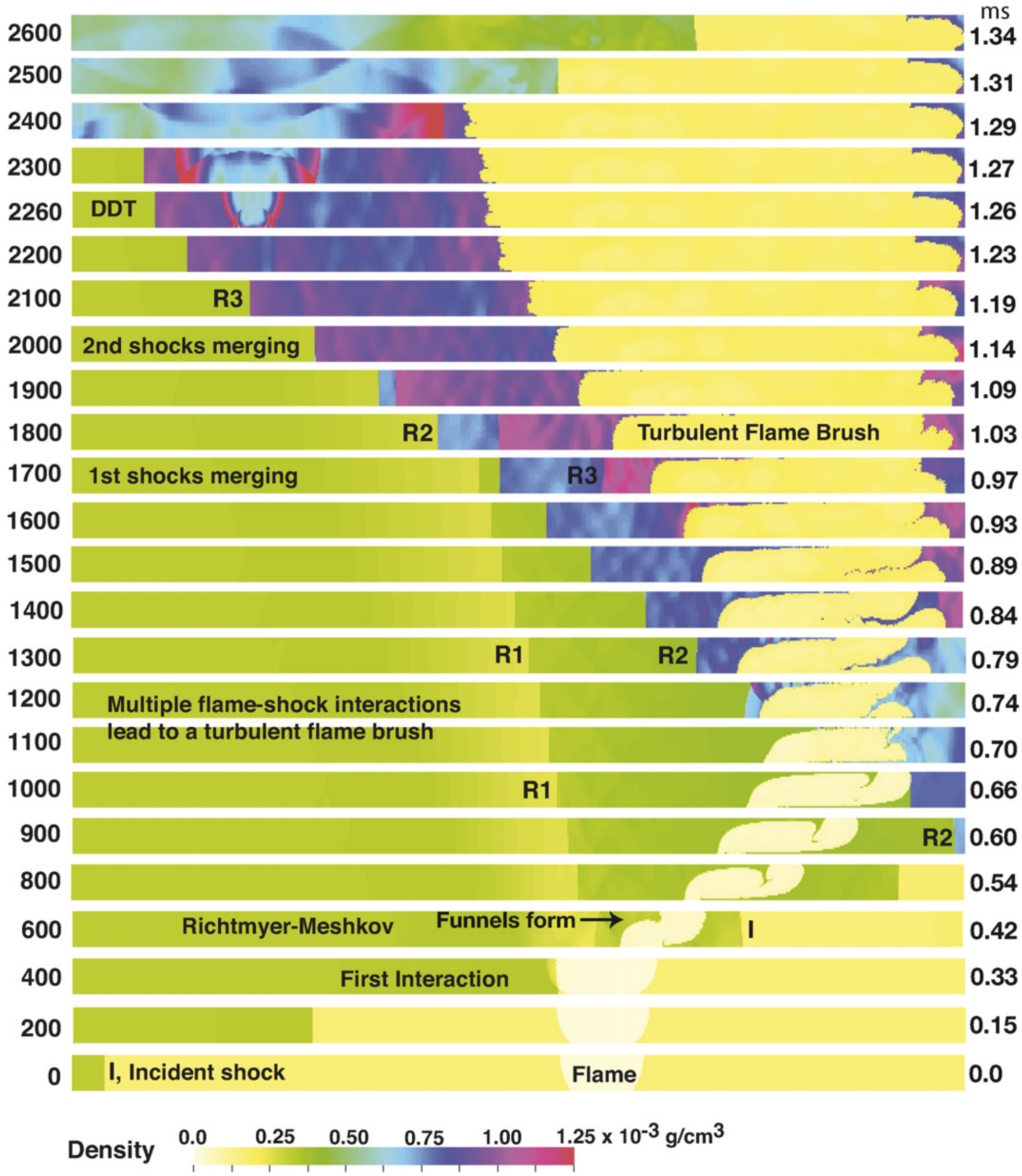

Fig. 7. Time sequence of density fields showing the overall evolution of a Mach 1.5 incident shock interacting with a low-pressure acetylene–air flame, corresponding to the initial and boundary conditions in Fig. 6. The computational domain for each frame is 32 cm by 1 cm. (The vertical scale is stretched by a factor of 1.28.) Time steps shown on the left side and physical times shown on the right side. Note that time differences between frames are not equally spaced, but are clustered near the DDT event starting at step 2200. Incident shock, I; reflected shocks, R1, R2, R3.

step 200. As the incident shock I interacted with the left side of the flame, an RM instability on the largest-scale was triggered by the overall curvature of the flame, and RM instabilities on the small scales were triggered by the small-scale perturbations of the flame surface. The small-scale RM structures quickly burned out and disappeared as the flame grew. The large-scale RM instability, however, resulted in a funnel of unburned material that penetrated the flame. When the shock emerged from the right side of the flame, it triggered an inverse RM funnel.

Since the shock interaction with the curved flame generates a shear flow, the small-scale perturbations triggered the Kelvin–Helmholtz (KH) instability along the surface of the flame. The small-scale KH instabilities also eventually burned out as the flame grew. The effects of all of these interactions was to increase the surface area of the flame. The energy re-

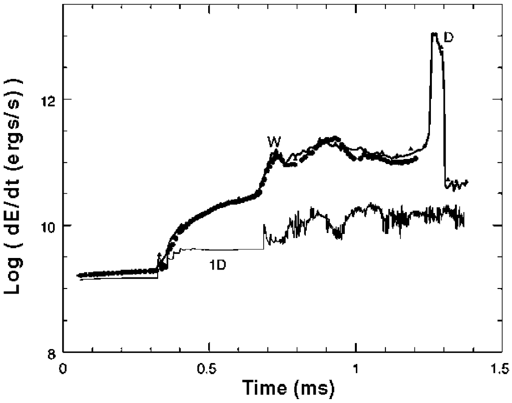

Fig. 8. Energy-release rate as a function of time for the $M_s = 1.5$ incident shock interacting with an acetylene–air flame, as shown in Figs. 6 and 7 [2]. The two-dimensional computations were performed with three different resolutions (solid line and dots superimposed). The letters indicate the onset of flame interaction with R3 (W) and DDT (D). One-dimensional results were obtained for initial conditions representative of the centerline of the two-dimensional problem.

lease in the system increased as a result of the increase in both the surface area of the flame and density of the background material.

By step 900, the surface area of the flame had increased substantially and the RM funnels had penetrated deeply into the flame region. The reflected shock R2 began to interact with the flame at step 1000. This created another funnel that had penetrated deeply into the flame by step 1300. R2 moved much faster in the burned material than in material in the funnels, which created a sequence of small oblique shocks, shear flows, and instabilities at the surface of the funnels. As a result, the funnels were compressed, broke up, and were quickly incinerated. This caused a burst of energy release in the system and generated intense pressure waves and shocks that moved through the entire system.

The shock R3 is another reflected shock that passed through the flame and finally emerged. The same overall process was repeated. R3 triggered another funnel, there were more instabilities and more fluctuations generated, and there was another rapid increase in energy release. Steps 1300 through 1600 show the disintegration of the funnel as R3 propagates along it. The funnel is essentially burned out by step 1700.

Thus, there was a sequence of shocks and rarefactions, including oblique and transverse waves, moving back and forth through the flame. This system of multiple shocks and rarefactions continually distorted the flame, increased the surface area, and thus maintained a high energy-release rate in the system. If these waves ceased to exist, the perturbations would have stopped, and the energy-release rate would decrease.

Fig. 8 shows that the energy-release rate begins to increase at 0.35 ms, initially due to the interactions with the incident shock and R2. Then it increases again at 0.7 ms as the flame interacts with R3 (marked W). The figure shows that the total energy release is about twenty times larger than in a comparable one-dimensional case, and it is maintained for a long time due to repeated shock–flame interactions. Finally, a detonation occurs (marked D) at approximately 1.25 ms. The one-dimensional problem also shows increases in energy release due to the shock–flame interactions. This increase is related to the compression of the material only.

6.2.2. *Transition to detonation*

The region behind R3 was very noisy, as is shown by the level of density fluctuations behind R3 between steps 1800 and 2200. DDT occurred between steps 2200 and 2260, just after several hot spots—regions of lower density and increased rate of energy generation—developed behind R3. A detailed analysis of these hot spots and their subsequent explosion [2,4–6] showed that this hot-spot ignition process is essentially the Zeldovich gradient mechanism. There is a gradient of reactivity (or chemical induction time τ_c) in the unreacted material, the material spontaneously ignites at the location of the minimum τ_c, and the reaction propagates in the direction of the gradient in τ_c. The reaction spreads as a spontaneous wave that can become a detonation wave or produce a flame and a decoupled shock, depending on the gradient profile. These computations were checked by performing extensive numerical-resolution tests, as described in [2].

6.3. *Effects of boundary layers on shock–flame interactions and DDT*

Real systems have boundaries and boundary layers that, in some circumstances, can have major, even controlling effects on the flow. Here we show that boundary layers can have a significant influence on shock–flame interactions and the subsequent transition to a detonation. To better explain the rather complicated phenomena that we observe in reactive systems in the presence of boundary layers, we first consider an inert system.

6.3.1. *Reflected shocks and boundary layers*

As a shock propagates down a channel, it leaves behind a boundary layer that grows in time. When this shock reflects from an end wall, it interacts with the boundary layer it created and forms a bifurcated

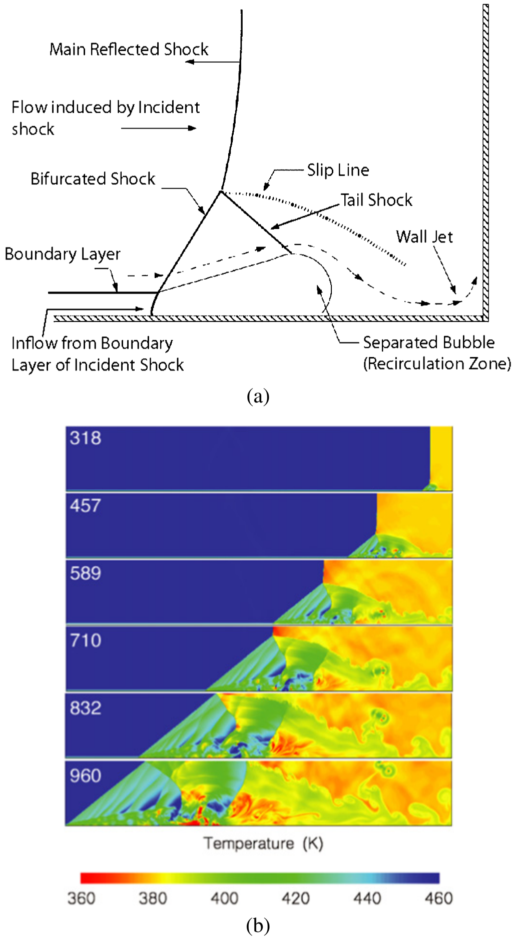

Fig. 9. (a) Schematic of the interaction between a reflected shock and a boundary layer in an inert fluid [9,11]. (b) Sequence of temperature distributions from computations showing the development of an inert bifurcated structure behind the reflected shock in an ethylene–air mixture for $M_S = 1.9$. Frames show a part of the computational domain, 22.8 cm by 3.8 cm, adjacent to the end wall (right boundary). The lower boundary is a no-slip wall, the upper boundary is a symmetry plane. Time (μs) is shown in the upper left corner.

shock structure. Interactions of shocks and boundary layers, resulting in shock bifurcations, have been studied experimentally (see, for example, [84–87]), theoretically (see [84,88,89]), and computationally [87,90–92]. A schematic of the a bifurcated shock complex is shown in Fig. 9a. The structure consists of the main reflected shock, an oblique leading shock (the bifurcated foot), a tail shock, a recirculation region (often called the "separated bubble"), and a wall jet at the end wall. As the material in the boundary layer created by the incident shock enters the reflected shock, part of it is deflected upward and flows past the recirculation bubble, and part enters the bubble. The important parameters of the process are M_S and γ. Higher values M_S and lower values of γ result in larger shock bifurcations. Thus we expect the effect of bifurcations at walls to be important for hydrocarbon gases with relatively low values of γ.

Fig. 9b shows the development of the reflected shock in an ethylene–air mixture, as computed with the ethylene–air model defined in Table 3. When the incident shock with $M_S = 1.9$ reached the end wall, the maximum boundary-layer thickness was 0.1 cm and the temperature at the bottom wall was about 24 K higher than in the bulk flow. As the shock reflected from the end wall, a bifurcated-shock complex develops. As the complex moved through the system, it left behind a number of vortices, weaker shocks, slip lines, and a relatively cold wall jet (318–589 μs). The bifurcated structure grew and quickly became tens of times larger than the original boundary layer created by the incident shock. When the foot reached the symmetry line of the shock tube, two feet collided and formed a regular reflection (832 μs). In this case, the incident shock was weak to cause any noticeable energy release by the time the reflected shock leaves the computational domain.

6.3.2. Effects of boundary layers on shock–flame interactions

The computations of shock–flame interactions in the presence of boundary layers (Set 5 in Table 1) were also based on a series of experiments by Thomas et al. [39], but here a single spark was used to ignite a flame near the end wall of a shock tube filled with a low-pressure ethylene–air mixture. A schematic of the computational domain (based on the experiments) is given in Fig. 10. For two-dimensional calculations, one-half of the system was simulated, although some simulations of the full two-dimensional system were done to test the effects of the otherwise imposed symmetry.

First consider the sequence in Fig. 11a, which is taken from a simulation with free-slip boundaries that suppressed the formation of a boundary layer. The first frame at 0 μs shows the initial conditions, a planar incident shock I moving from the left to the right, and the flame F. The sequence of frames, with time increasing from top to bottom, shows the incident shock I moving through and distorting the flame, reflecting from the back wall, and then the reflected shock R2 passing through and further distorting the flame. Hot spots form in unreacted material, and eventually two of the hot spots undergo transitions to detonations at 593 and 608 μs. The evolving structure of this flow has many similarities to the acetylene–air simulations discussed above.

The sequence in Fig. 11b shows the development of the flow for the same mixture and value of M_S,

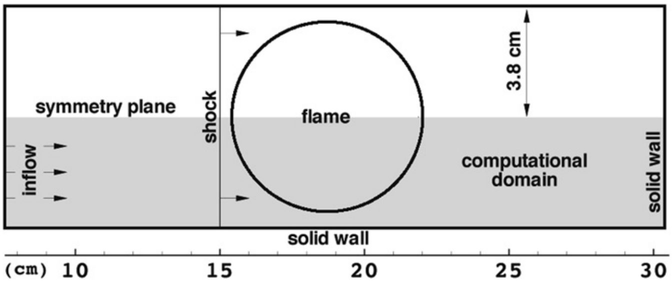

Fig. 10. Schematic diagram showing the computational domain and the initial and boundary conditions for the two-dimensional single-spark ethylene computations [9].

but now for the case with a no-slip wall that allows a boundary layer to form. The boundary layer behind the incident shock is about 0.1 cm thick and is not visible in these frames. From the beginning of the simulation to about 225 µs, the flow development is practically the same as it was for the case with free-slip walls. Boundary-layer effects do become apparent at 171 µs when R1 begins to form a weak bifurcated structure B1, but B1 does not affect the flame until a later time. Another bifurcated structure B2 (not shown) begins to grow immediately after the incident shock reflects from the back wall, but it is quickly destroyed by a strong oblique shock coming out of the flame. Multiple reflections of oblique shocks and rarefaction waves inside the thin layer of unreacted material between the flame surface and the bottom wall prevent the formation of new bifurcated structures until about 340 µs.

The flame remains essentially unaffected by boundary-layer phenomena until 363 µs. By that time, R2 has passed through the flame, and a new strong bifurcated structure B3 begins to develop. Details of this development can be seen in Fig. 12, which is an enlargement of the regions around the bifurcation. In addition to the density, Fig. 12 shows the temperature gradient and pressure. When a bifurcated foot forms and grows, a recirculation region forms and grows behind it. Near the bottom wall, the flow in the recirculation region is moving towards the shock. The flame, which almost touches the bottom wall and moves with the flow behind the shock, penetrates the recirculation region. The flame approaches the shock first as a thin jet along the wall, and then quickly spreads inside the recirculation zone. The energy released by the flame in the recirculation region accelerates the growth of the bifurcated foot until the top of the foot reaches the symmetry plane (top boundary of the computational domain) and a forms a Mach reflection at the top boundary by 424 µs (Fig. 11b).

6.3.3. The reactive shock bifurcation and the DDT

The result of the complex interactions described above is the reactive shock bifurcation enlarged in Fig. 13. This structure involves an oblique shock and a flame (marked in Fig. 13a with a “1” and “2,” respectively). The slope of the oblique shock is increased with respect to the inert case shown in Fig. 9b, and this causes a Mach reflection (“3”) at the top boundary instead of a regular reflection observed for the inert case. At this scale, it appears that the shock touches the flame at the bottom boundary. An enlargement of this regions (now shown here) indicates that the shock *almost* touches the flame. The flame surface coincides with the boundary of the recirculation region.

The velocity of the material inside the tip of the flame is approximately the same as the velocity of the bifurcated shock and is practically independent of the laminar flame speed or energy release; the burned gas just moves with the flow. Away from the tip, the velocity of the unburned material behind the oblique shock is different from the velocity of the burned gas in the recirculation region. Thus a slip line forms along the flame surface. Vortices generated by the KH instability along the slip line grow with distance from the bottom wall and increase the surface area of the flame. The upper part of the flame interacts with the flow of unreacted material behind the Mach stem. This flow disrupts the flame surface and prevents the flame from reaching the symmetry plane. As a result, a relatively thick funnel of unreacted material with a very convoluted surface forms near the top boundary and grows as the shock propagates along the tube (see Fig. 11b, 424 and 444 µs).

The structure of the reactive shock bifurcation is not quite steady-state. The surface area of the flame increases as the funnel grows, thus increasing the energy-release rate in the system. The energy release gradually increases the strength of the bifurcated shock and the Mach stem. Eventually, the temperature behind the Mach stem becomes high enough to ignite the mixture (Fig. 14). Ignition produces several hot spots, spontaneous waves, and residual flames that grow quickly, interact with vortices, and eventually trigger a detonation (D1 in Fig. 11b). The detonation wave propagates in all directions, consuming the high-density unreacted material in the funnel and be-

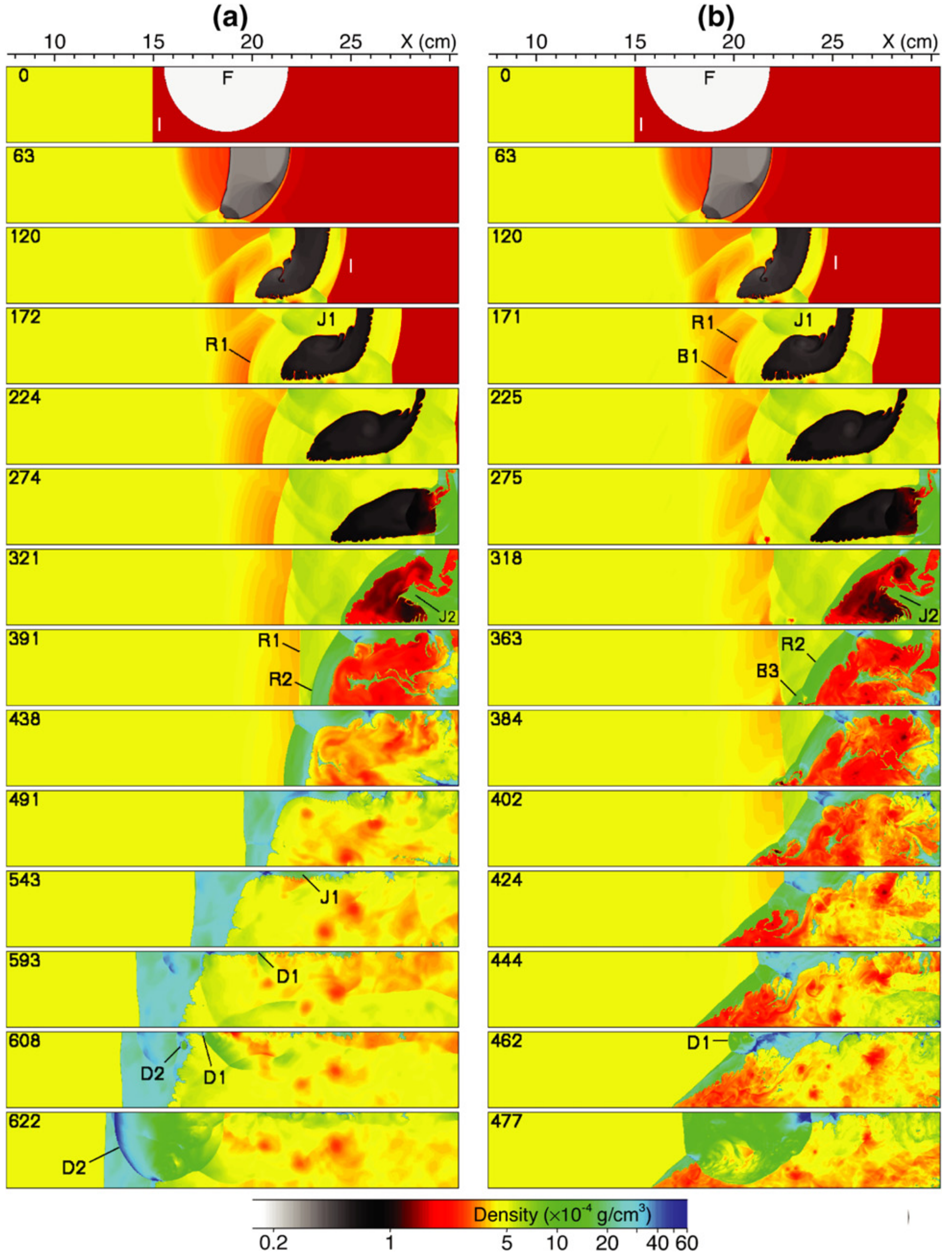

Fig. 11. Sequence of density fields showing the overall flow development for $M_S = 1.9$ (a) without boundary layers and (b) with boundary layers [9,11]. Time (μs) is given on the left side of each frame. The letters indicate the incident shock I, the flame F, reflected shocks R1 and R2, funnels of unreacted material J1 and J2, detonations D1 and D2, and bifurcated structures B1, B2, and B3.

hind the oblique shock. When the detonation enters the relatively low-density, unreacted material compressed only by the incident shock, it becomes unstable and forms transverse-wave structures. (Transverse waves are barely visible in Fig. 1 that was extracted from a higher-resolution computation performed for the same system.)

6.4. *Three-dimensional reactive shock bifurcations*

We were able to perform a limited number of three-dimensional simulations to determine how and if the results obtained in two-dimensional simulations carry over to three dimensions. There were several reasons to question two-dimensional results, includ-

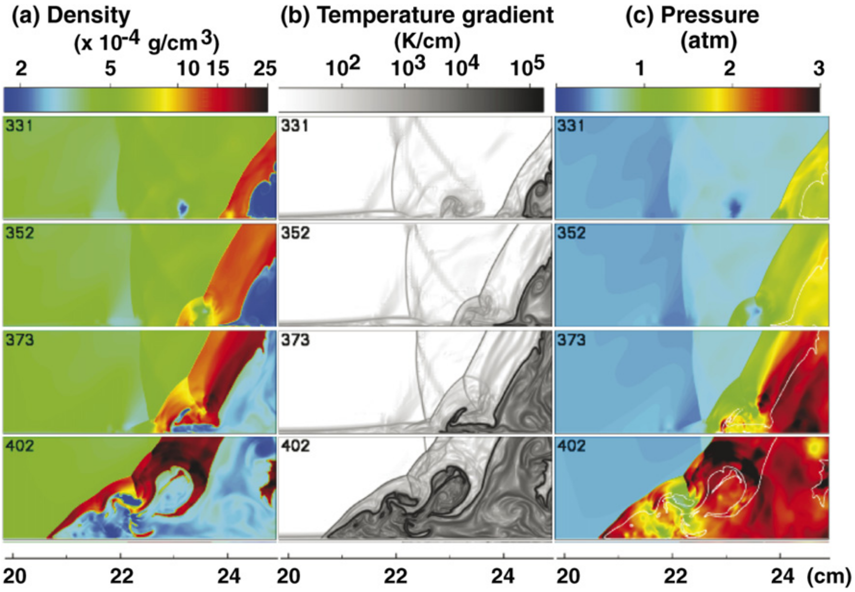

Fig. 12. Sequence of (a) density, (b) temperature gradient, and (c) pressure fields near the bottom wall showing the formation of the reactive bifurcated structure indicated as B3 in Fig. 11b [9,11]. Time (μs) is given on the upper left side of each frame.

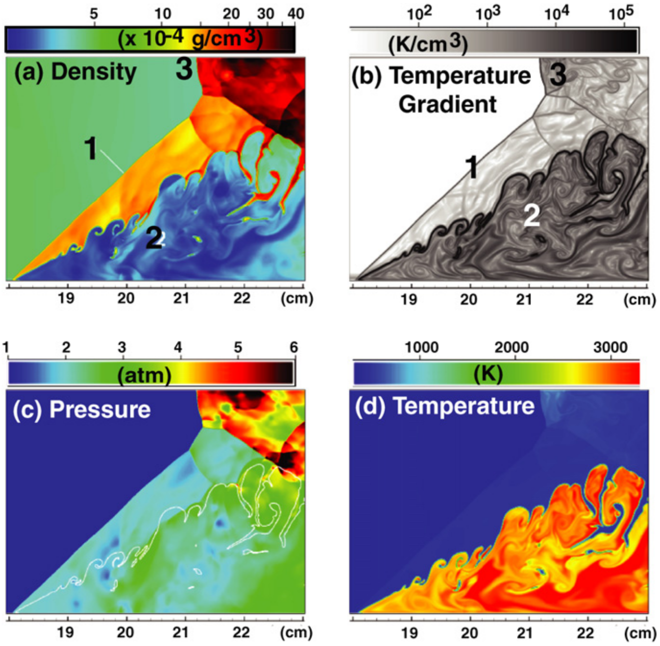

Fig. 13. (a) Density, (b) temperature gradient, (c) pressure, and (d) temperature fields showing the reactive shock bifurcation at 444 μs (B3 in Fig. 11b). The numbers indicate the bifurcated foot (1), the flame (2), and the Mach stem (3). The flame surface is indicated in the pressure frame by the superimposed white $Y = 0.5$ contour.

ing the basic differences in the behavior of turbulence and the added complexity of shocks and shock bifurcations in three dimensions. Here we briefly describe three-dimensional simulations of shock–flame interactions in a channel containing an ethylene–air mixture [10].

The three-dimensional computational setup shown in Fig. 15 is similar to the two-dimensional setup shown in Fig. 10. Symmetry boundary conditions are used to simulate one quarter of the system, and no-slip boundary conditions are applied along all walls. Fig. 16a shows the flow development through the time

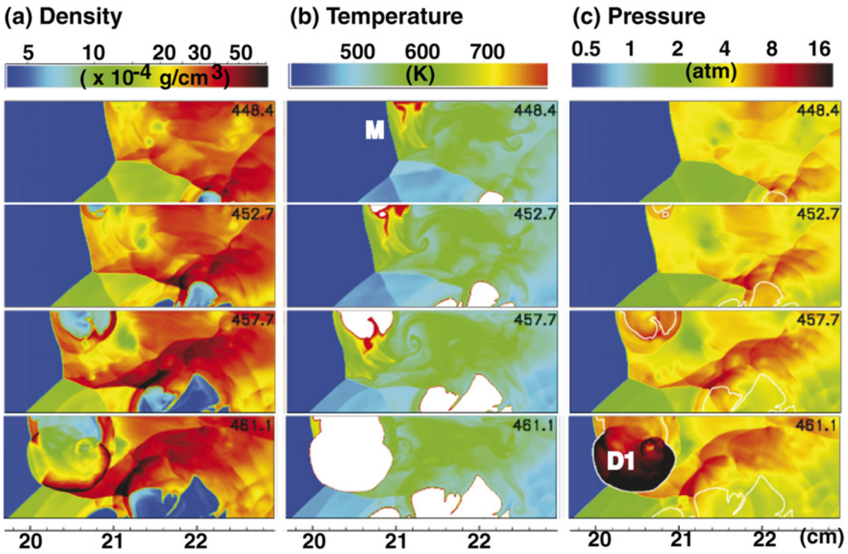

Fig. 14. Sequence of (a) density, (b) temperature, and (c) pressure fields, enlarged from the calculations shown in Fig. 11b, show DDT behind a Mach stem [9,11]. The flames are shown as white areas in the temperature frames. Flame surfaces (white $Y = 0.5$ contour) are shown in the pressure frames. Time (µs) is given on the upper right side of each frame. The detonation is indicated as D1 in Fig. 11b. M indicates the Mach stem.

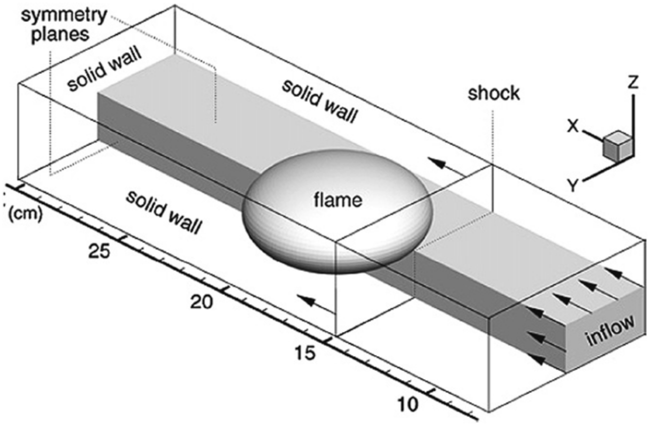

Fig. 15. Schematic diagram describing the initial and boundary conditions for the three-dimensional computation [10]. Gray box shows the computational domain.

sequence of images of the flame and shock surfaces. The incident planar shock moves along the x-axis and interacts with the flame. As in the two-dimensional calculations described above (Fig. 11b), the interaction is dominated by the Richtmyer–Meshkov instability, triggered by the flame curvature. The instability generates a large three-dimensional vortex that distorts the flame and creates a funnel of unreacted material in central parts of the shock tube near symmetry planes. On smaller scales, the RM instability creates small ripples on the flame surface. The interaction also distorts the initially planar shock that propagates through burned and unburned materials at different speeds. Oblique parts of the distorted shock reflect from side walls and interact again with the flame, creating more distortions.

As the flame continues to move with the flow, the incident shock reaches the end wall at 255 µs and reflects. The stronger reflected shock R moves back through the already perturbed flame and creates more distortions at different scales. The flame quickly develops a very convoluted surface and becomes turbulent. The energy release accelerates due to the increased surface area of the flame and the increased temperature and density of unburned material behind the reflected shock.

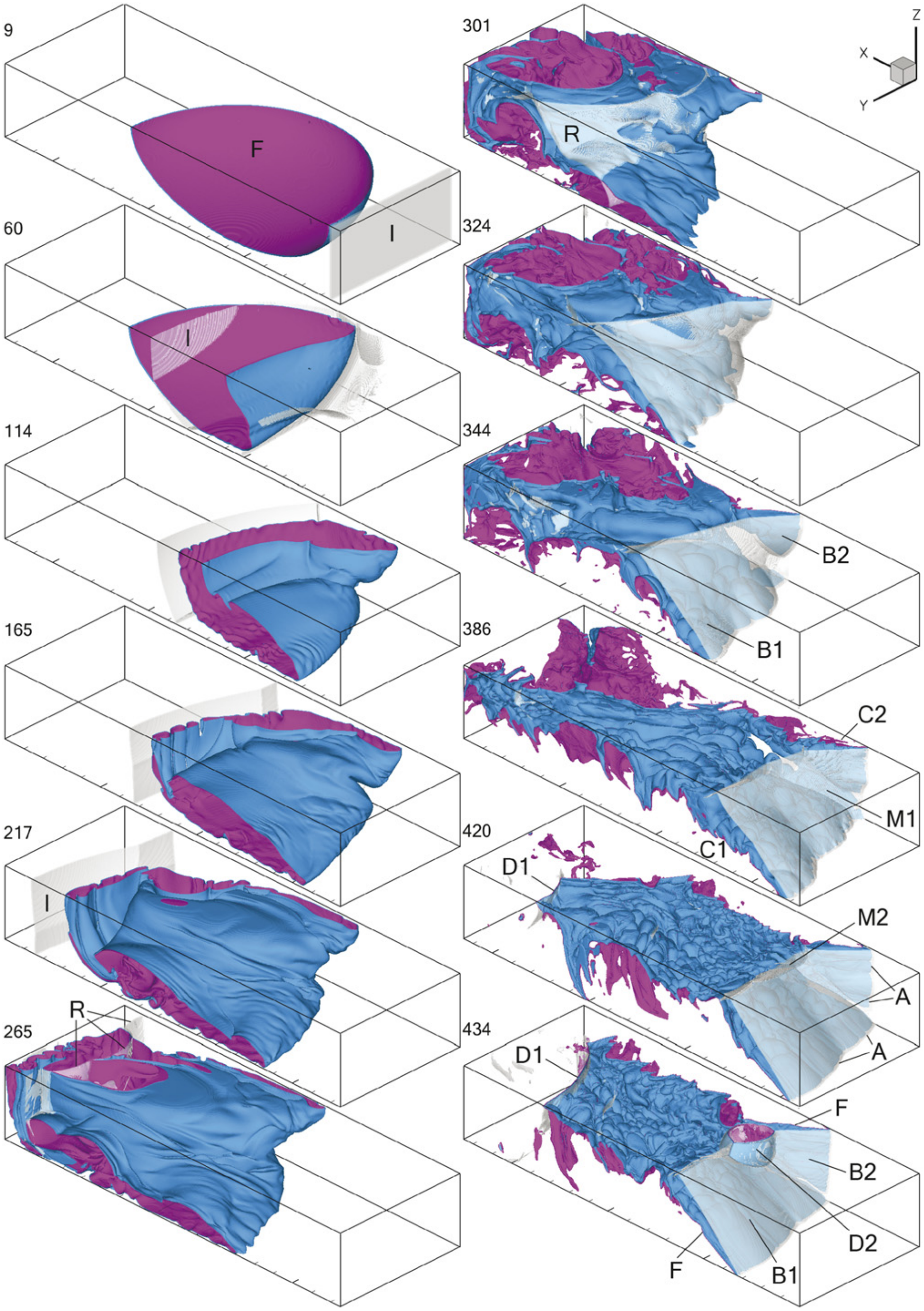

(a)

Fig. 16. Time sequence of (a) computed three-dimensional surfaces of flame (blue side faces unburned mixture; purple side faces burned gas) and shock (gray semitransparent), and (b) corresponding computational schlieren images calculated for x–y and x–z planes [10]. Time in µs is shown in the upper right corner of each frame. No-slip walls are at $y = 0$ and $z = 0$; opposite boundaries are symmetry planes. Each frame shows a 10.6-cm-long part of the computational domain adjacent to the end wall on the left ($x = 30.4$ cm) for 217–386 µs, and shifted 1.5–3 cm from the end wall for other times. The letters indicate the incident shock I (see 9, 60, and 217 µs), the flame surface F (see 9 and 434 µs), the reflected shock R (see 265 and 301 µs), the bifurcated shocks B1 and B2 (see 344 and 434 µs), the recirculation areas C1 and C2 (see 386 µs), the shock–flame attachment line A (see 420 µs), Mach stems M1 and M2 (see 386 and 420 µs), and detonations D1 (see 420 and 424 µs) and D2 (see 434 µs).

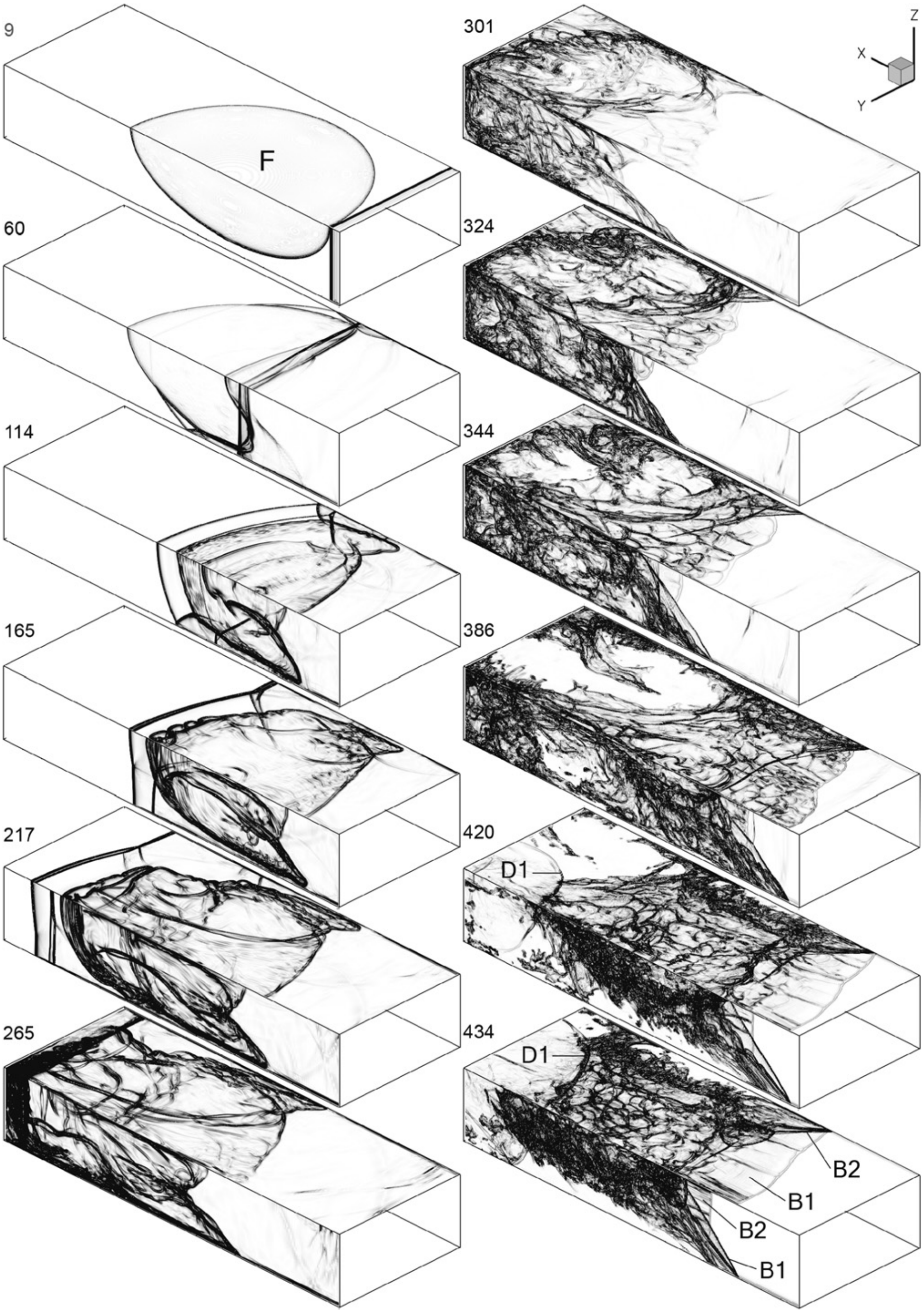

(b)

Fig. 16. (*continued*)

When the reflected shock crosses the flame and enters the unburned material upstream, it begins to interact with boundary layers that developed near the no-slip walls. These interactions result in shock bifurcations B1 and B2 that appear in Fig. 16a as oblique shocks propagating along the walls, $y = 0$ and $z = 0$. Shock bifurcations also create strong recirculation regions C1 and C2 near the walls. The recirculation flow entrains the flame that spreads through the recirculation region, approaches the bifurcated shock, and then attaches to it near the wall. The attachments first occurs near symmetry planes, where the initial flame surface was closest to no-slip walls. Then the attachment line approaches the corner $y = z = 0$ between these walls. The attachment line is rather irregular because the flame and the boundary layer behind the bifurcated shock are turbulent. Above the attachment line, the flame surface F coincides with a slip surface that forms behind the bifurcated shock. The KH instability that develops along this surface generates more turbulence.

The reactive bifurcated shocks propagate with a speed of about one-half D_{CJ} and interact with each other along the line that begins in the corner $y = z = 0$. The interaction between oblique shocks B1 and B2 produces an oblique Mach stem M1 that generates additional vorticity and locally increases the temperature of shock-compressed material. The oblique shocks are relatively weak, and therefore the oblique Mach stem is not strong enough to ignite the material.

DDT producing detonation D2 occurs when the bifurcated shock B1 attached to the wall $z = 0$ forms another Mach stem M2 near the symmetry plane $z = 1.9$, and this central Mach stem interacts with the oblique Mach stem M1 creating a hot spot. Another detonation D1 appeared earlier in the funnel, near the end wall, but it did not affect the formation of D2 behind two interacting Mach stems.

Computational schlieren images, Fig. 16b, were generated using the data shown in Fig. 16a and the simplified model for light propagation described in [10]. The light propagating along the z-axis produces an image in the x–y plane, and the light propagating along the y-axis produced images in the x–z plane. These images are shown in Fig. 16b on the corresponding walls of the same three-dimensional box that shows computational domain boundaries in Fig. 16a. The steepest density gradients that produce shadows in these images are in the reaction zone of the flame and inside shocks. White areas correspond to the parts of the computational domain where all the material is still unburned or burned completely. The flame and strong shocks are visible on these images, but we cannot see the full three-dimensional structure of the reactive bifurcated shocks in the two-dimensional images. For example, when the bifurcation forms on the wall $z = 0$, the x–y schlierens show a turbulent flame moving just behind a curved shock. The x–y images do not show that the shock is oblique and the flame is attached to it only near the wall. These details can be seen only from the y-direction that corresponds to x–z images.

These computations show that the three-dimensional reactive shock bifurcations that developed on the channel walls have essentially the same features and behavior as the two-dimensional structures described earlier. This includes entrainment of a the flame by a recirculation zone behind a bifurcated shock, development of the KH instability on the reactive slip surface behind the bifurcated shock, fast growth of the bifurcated structure, propagation of the reactive bifurcated structure at about half D_{CJ}, and the formation of a Mach stem when the bifurcated structure grows to the size of the channel.

The main difference between two- and three-dimensional results is related to the presence of the second no-slip wall in a rectangular channel. Two reactive bifurcated shocks forming on adjacent walls interact with each other and produce an oblique Mach stem between two oblique shocks. The oblique Mach stem then interacts with the central Mach stem, and this interaction forms a hot spot that leads to a detonation initiation. Other differences appear due to an additional degree of freedom for the flame and shock dynamics in three dimensions. For example, the nonplanar bifurcated shocks are perturbed by transverse waves in the third dimension, the flame spreads nonuniformly across the recirculation zone in the third dimension, and there is an irregular, dynamically changing line of attachment of the a flame to the bifurcated shock near the wall. The third dimension also makes it possible for vortical structures to break down and transfer turbulent energy to the smaller scales, and results in an increased growth rate for the RM instability. This affects the turbulent flame development, but has a little influence on the structure and dynamics of shock bifurcations. The nature of the turbulence that dominates this types of flows with shocks and flames is discussed further in Section 10 in the section on nonequilibrium turbulence.

7. The strange wave and related phenomena

Shock–flame experiments reported by Scarinci et al. [37] showed the development of a reflected shock wave, as we saw in Fig. 7, for example, in which the flow directly behind the shock appeared turbulent. For a significant time, this wave traveled at an essentially constant speed of about half the CJ detonation velocity, and the turbulent region remained attached to the shock. The state of the material, the nature of the turbulence behind this wave, and the mechanism by which this wave is supported were not known. There had been some debate as to the nature and structure of this wave, whether or not the material behind the front was burned, thus producing a “supersonic flame,” or what state the wave could be in if it were not burned. We called this wave a “strange wave” and determining what it was became a quest.

7.1. The origin of the strange wave

The earliest studies we did of a single interaction of a shock and a curved flame (for example, in Fig. 5) showed that this interaction alone has a relatively mild effect on the increase in the burning rate [1]. The effect was stronger for multiple shock–flame interactions (Fig. 7), which continually distorted the flame and increased its surface area, and so increased the energy-release rate. The increased heat release amplified the shocks and eventually led to the formation of a final reflected shock. This final shock had some characteristics in common with the strange wave. Thus we first tried to find an interpretation for this strange wave based on the computations shown in Fig. 7.

The speed and the strength of the reflected wave R3 in Fig. 7 were similar to those of the strange wave observed experimentally. The final reflected shock that emerged from the flame brush, R3, traveled at approximately 900 m/s relative to the material ahead of the shock. This speed is approximately half of the Chapman–Jouguet velocity D_{CJ}. The pressure behind the wave was about 10 times the initial pressure, which corresponded to the pressure of constant volume burning of the original material. Before the transition to a detonation, R3 propagated for a substantial length of time (about 0.3 ms) without decaying or growing in strength. Computations with a weaker incident shock, $M_{\mathrm{S}} = 1.4$, also generated a reflected shock wave with similar characteristics. Again, the velocity was about half D_{CJ} and the postshock pressure was comparable to that of a constant volume explosion. In this case, the shock wave lasted longer and there was no transition to a detonation.

In both the $M_{\mathrm{S}} = 1.4$ and 1.5 simulations, there were high levels of density and pressure perturbations behind this shock. These perturbations were generated by the turbulent combustion and shock reflections in the flame brush, and they propagated through the unburned shocked material. Thus we suggested that the strange wave might be one of the reflected shocks that emerge from the flame. Behind this shock, the material was highly perturbed, and there were significant fluctuations in its properties. Extension to a real system could mean that the material is turbulent enough to account for the strange wave [2].

Then in a more recent paper, Thomas et al. [39] described measurements indicating that the fluid behind the strange wave was not only turbulent, but had burned. This fact was not consistent with the results shown in Fig. 7. The mystery was not resolved until further simulations, such as those shown in Fig. 11, were done to examine the effects of boundary layers [9]. We then learned that the leading edge of the strange wave may be closely followed by the tip of flame attached to a vortex moving in a complicated boundary layer behind the reflected shock.

The strange wave was observed in experiments using schlieren photography, which produces two-dimensional images by looking through the boundary layer and across the channel. Assuming the entire wall of the detonation tube is covered with a boundary layer that causes the bifurcation of the reflected shock and produces the reactive bifurcated structure, the schlieren image will show a turbulent flame following, and seemingly attached to, the leading shock. Thus we now believe that the structure of the strange wave is that of a reactive shock bifurcation. This explanation is consistent with the facts that there are significant chemical reactions in the experimentally observed strange wave and that the strange wave is not a detonation. Numerical schlieren images computed from three-dimensional simulations, shown in Fig. 16b, are also consistent with experimental schlieren images [37,39].

As a final point, we note that not all of the experiments discussed by Thomas et al. [39] show strange waves. They were not seen when the initial flame was relatively small and far from the walls. This difference between initially large and small flames is consistent with our results, which show that, for a flame to interact with the recirculation region, and for the reactive shock bifurcation to form, the flame has to be close enough to the wall to be entrained by the vortices at the boundary.

7.2. Wakes

Another series of simulations of shock–flame interactions were performed for flows with embedded obstacles. These were motivated by the presence of the spark igniter itself, which protruded into the flow, and by observations of flows around pieces of diaphragms that were left on the channel walls from previous experiments [39]. The simulations were done for the ethylene–air mixture and for various sizes of embedded obstacles [11,15]. Note that the simulations described below were intentionally performed without boundary layers and with an obstacle placed in the middle of the channel in order to isolate the wake effect. The computational setup was the same as shown in Fig. 10, except for the obstacle that was located between the initial shocks and the flame. Flow development corresponding to $M_{\mathrm{S}} = 1.8$ and a 0.475-cm square obstacle are shown by the sequence of density frames in Fig. 17.

The top left frame of Fig. 17 shows the incident shock I and the flame F shortly after the initial shock–flame interaction. At the beginning, the flow development is similar to the case without obstacles and boundary layers, as in the early times shown in

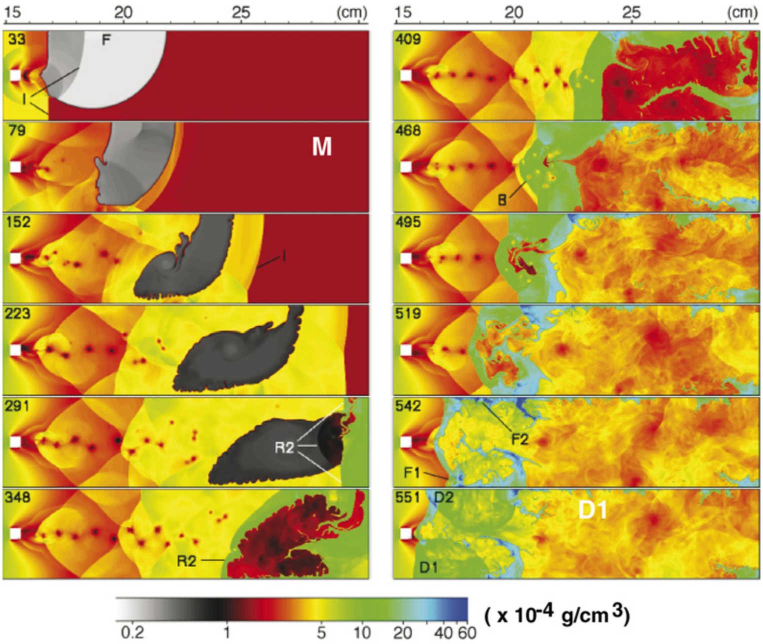

Fig. 17. Time sequence of density fields showing shock–flame interactions in the presence of an obstacle (shown as a white square) for $M_S = 1.8$ [11,15]. Upper, lower, and right boundaries are free-slip walls. Time (μs) is given on the upper left side of each frame. The letters indicate the incident shock I (see 33 and 152 μs), the original flame F (see 33 μs), the reflected shock R2 (see 291 and 348 μs), the bifurcated wedge B (see 468 μs), the new flames F1 and F2 (see 542 μs), and the detonations D1 and D2 (see 551 μs).

Fig. 11a. The obstacle has a relatively small effect initially as it diffracts the incident shock before its interaction with the flame. The major effect, however, occurs when the reflected shock R2 exits the flame (348 μs), interacts with the wake, and forms a bifurcated wedge B (468 μs). This process is shown in detail in Fig. 18. The wedge grows and forms Mach reflections at the side walls, thus increasing the post-shock temperature in the vicinity of the walls. The recirculation flow develops behind the wedge and begins to interact with the flame. The part of the flame that enters the recirculation region becomes entrained by the flow and quickly spreads inside this region. The vortices, which originate in the wake and pass through the bifurcated shock, also participate in the recirculation flow and interact with the flame. As the flame approaches the bifurcated wedge, it spreads sideways to the walls with the flow deflected by the oblique shocks. The energy released by the flame increases the strength of all the shocks including the Mach stems at the walls.

Eventually, the temperature of the shock-compressed material surrounding the flame increases to the point where the mixture ignites, almost simultaneously, at two different locations. These ignition points appear behind the Mach stem at the bottom wall, and between the flame and the symmetry line at the top. The resulting new flames are seen at 541 and 542 μs in Fig. 18. Detonations D1 and D2 appear at both locations shortly after ignition. In comparison, the case with the same incident shock strength ($M_S = 1.8$), but without obstacles and boundary layers (figure not shown here), did not produce DDT within the length of the channel.

The numerical results show that the presence of a wake in the flow can have a significant influence on flame acceleration behind the reflected shocks. Similar flame acceleration was observed in shock-tube experiments [39] when wakes were created either by a thick ignition rod or by a fragment of the diaphragm that remained on the wall of the window section after a previous experiment. The wake effect described here is significant when the obstacle is large enough to create a long wake that allows the bifurcated structure to develop and to entrain the flame. In calculations with a small obstacle (0.12 × 0.12 cm), the wake was not sufficiently long to affect the flame. The fact that the effect was not observed for thin ignition rods agrees qualitatively with the numerical results for small obstacles. In experiments, where the obstacles were located at the walls of the shock tube, a combination of wake effects and boundary-layer effects occurred.

The mechanism by which a flame accelerates behind a shock that is propagating through a wake is similar to the boundary-layer effect. Either a wake or

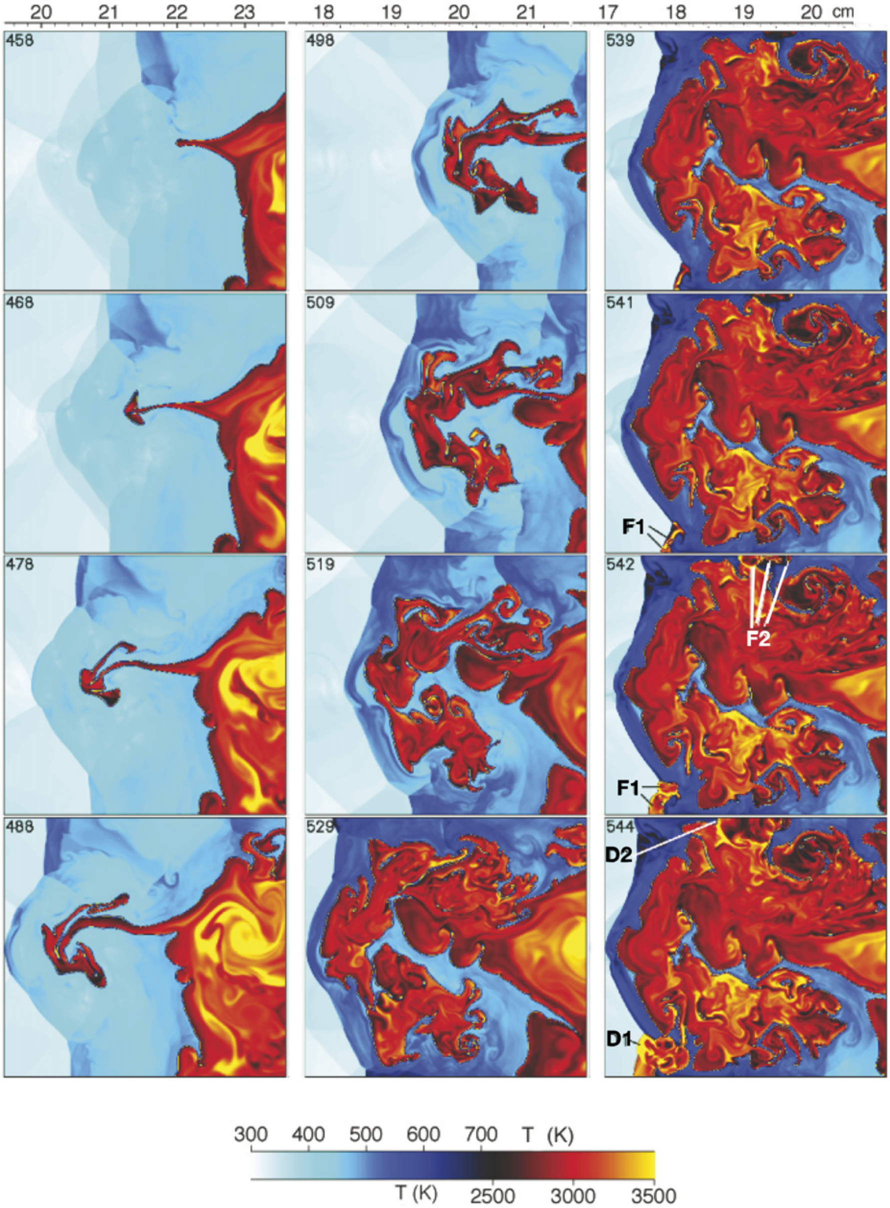

Fig. 18. Formation of the reactive bifurcated structure from a wake and subsequent DDT [11,15]. These frames are produced from the calculation shown in Fig. 17. Two temperature scales show the temperature in the unreacted material and the burned gas. Time (μs) is given on the upper left side of each frame. The letters indicate the new flames F1 and F2 (see 541 and 542 μs), and the detonations D1 and D2 (see 544 μs).

a boundary layer contains a velocity gradient that results in bifurcation of a shock moving through this gradient. The wake-induced inert bifurcated structure, enlarged in Fig. 19, has almost the same features as the bifurcated structure induced by a boundary layer, as shown in Fig. 9. Either bifurcation creates a recirculation flow that entrains the flame, thus accelerating it. As the flame approaches the shock, the bifurcated foot or wedge grows, reflects from a side wall, and forms a Mach stem that can create conditions for ignition and DDT. Further details are given in [11,15].

8. The role and structure of hot spots

In all of the simulations presented in this paper, the detonations that developed always arose from hot spots (or ignition centers) in unreacted material. Now we focus on one typical hot spot and show that the

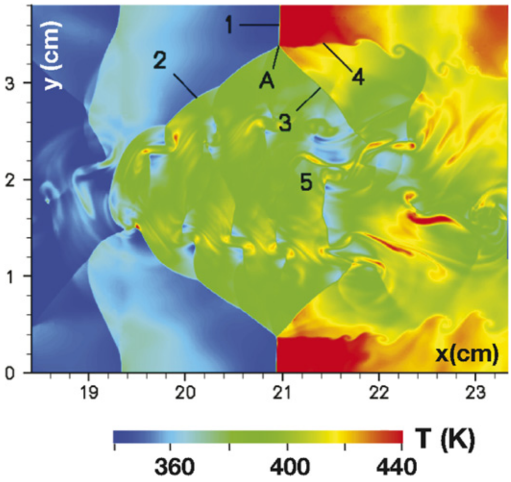

Fig. 19. Temperature field in the vicinity of the bifurcated reflected shock propagating from the right to the left through a wake in an inert ethylene–air mixture for $M_s = 1.8$ [11,15]. Legend: 1, reflected shock; 2, bifurcated foot; 3, tail shock; 4, slip line; 5, recirculation region; A, triple point. (Compare to Fig. 9a.)

conditions in this hot spot are consistent with the Zeldovich gradient mechanism for propagation of spontaneous reaction waves that could undergo transition to a detonation.

Consider Fig. 7, which shows density as a function of time for the simulation of a shock–flame interaction in an acetylene–air mixture with symmetric boundary conditions, and therefore no complications from boundary effects [2]. The region where hot spots develop into a detonation is seen at step 2260 (1.26 ms) and is located between the turbulent flame and the reflected shock. Details of this transition are shown in Fig. 20. The energy-release rate in Fig. 20a, and the density in Figs. 20b and 20c, allow us to track the development of reaction fronts and shocks.

The distribution of the induction time, τ_c, as computed from the Frank–Kamenetskii approximation [93], is shown in Fig. 21a for the same time (1.2512 ms) as the first frame in Fig. 20. Given the chemical model we are using (Eq. (7)), the induction time is

$$\tau_c = \left(\frac{C_V T}{Aq\rho Y}\right)\left(\frac{RT}{Q}\right)\exp\left(\frac{Q}{RT}\right), \qquad (10)$$

[6], where $C_V = R/M(\gamma - 1)$ is the specific heat at constant volume. (The accuracy of this approximation is discussed in [2].) There are several hot spots and a gradient of τ_c at each hot spot. The explosion begins in the location of minimum induction time in the upper hot spot (1.2512 ms), and it propagates as a spontaneous wave with a speed $D_{sp} = |\nabla\tau_c|^{-1}$. Fig. 21b shows the predicted D_{sp} computed from τ_c. The values of D_{sp} are highest where $\nabla\tau_c$ is lowest. In the hot spots, $D_{sp} > D_{CJ}$. The contour $D_{sp} = D_{CJ}$ shown in Fig. 21b indicates the boundaries of the spontaneous flame region. The value of $D_{CJ} = 1.97$ km/s was calculated for the background material, which has been shocked, compressed to $\simeq$1.64 atm, and heated to $\simeq$780 K. Because the gradient is different in different directions, the shape of the spontaneous region is not circular.

Fig. 20 shows that the shock wave first appears at 1.2522 ms on the right side of the hot spot, where the gradient of τ_c is the steepest (Fig. 21). The wave on the left is smooth, which is typical of spontaneous waves discussed extensively in the literature (for example, [30,32,60–62]). At 1.2527 ms, the spontaneous waves have already undergone transition to detonation and there are two shocks propagating in opposite directions. Closer inspection of the results shows that shock waves emerge on the predicted $D_{sp} = D_{CJ}$ boundary, shown in Fig. 21. The second hot spot ignites later and proceeds through the same sequence of events.

These results are consistent with the gradient mechanism for ignition, according to which there is no shock present at the initial stage of spontaneous wave propagation. The velocity of the spontaneous wave is initially greater than D_{CJ} and decreases as the reaction spreads. When the velocity has decreased to about D_{CJ}, a shock wave emerges and the spontaneous wave undergoes a smooth transition to a detonation. This transition does not occur simultaneously in all directions; each direction is essentially independent of the other because $D_{sp} > D_{CJ} > c_s$, where c_s is the local sound speed.

The description given of the ignition event shown in Figs. 20 and 21 was limited because the data was extracted from a large complex simulation. We can take this analysis further by isolating the conditions in the initial gradient in reactivity and considering an isolated asymmetric hot spot. (This analysis was developed with A.M. Khokhlov and reported in more detail in [6].)

Suppose that there is a nonuniform distribution of temperature, $T = T(\mathbf{r})$, where $\mathbf{r}$ is a position inside a hot spot. It is not difficult to imagine how a nonuniform distribution could be created in a highly compressible flow with pressure fluctuations, shocks, shears, turbulence, etc. In such complex, dynamic flows, we can expect gradients with almost any spatial shape. Furthermore, as we have seen in some cases, the gradient can be altered by interactions with weak shocks and pressure waves while the spontaneous waves are developing. Thus the proper description of the temperature distribution is really $T = T(\mathbf{r}, t)$. We consider, however, an idealized case, $T = T(\mathbf{r})$, that leads to the spatial distribution of induction time $\tau_c = \tau_c(\mathbf{r})$. The explosion of a hot spot begins at the

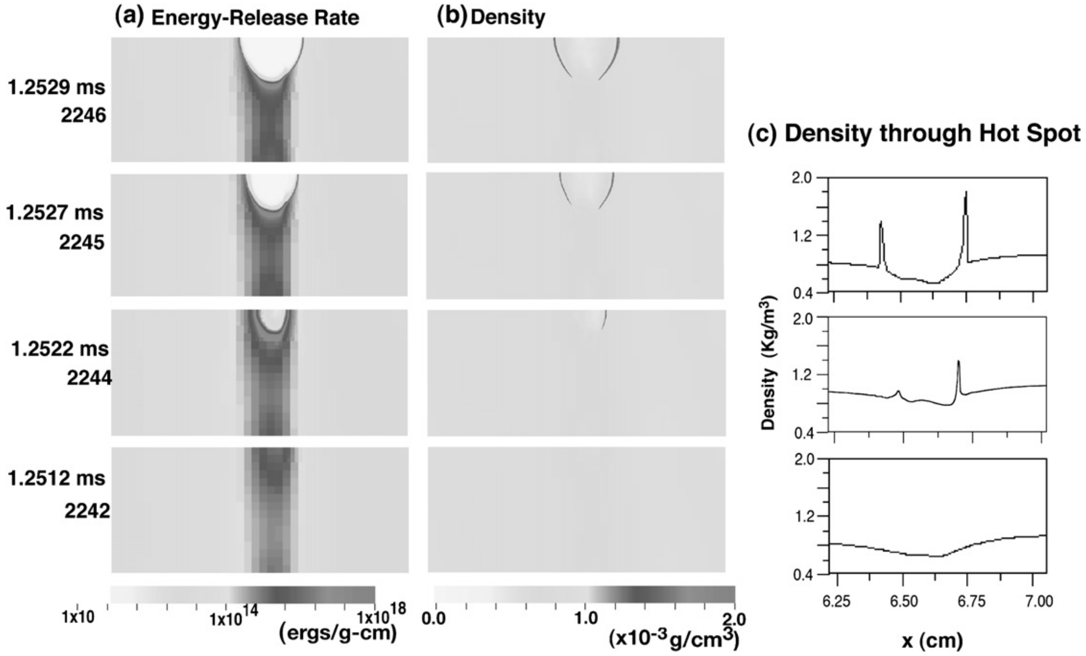

Fig. 20. Enlargement of the region of hot-spot ignition for multispark acetylene–air calculation at $M_s = 1.5$ [2,4,5]. (a) Energy-release rate. (b) Density. Frames shown are 32 computational time steps apart, $x = 5.3$–7.7 cm, $y = 0.0$–1.0 cm. (c) Density as a function of x for $y = 0.73$ cm through the igniting hot spot.

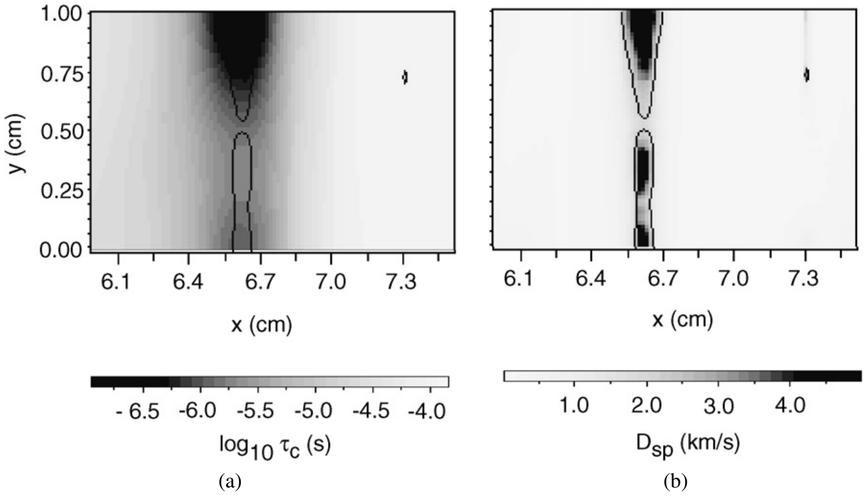

(a) (b)

Fig. 21. Enlargement of the region of hot-spot ignition for multispark acetylene–air calculation at $M_s = 1.5$ [2,4,5]. Distribution of (a) chemical induction time τ_c and (b) the predicted spontaneous wave velocity D_{sp} for 1.2512 ms in Fig. 20.

point of minimum τ_c and then spreads at varying local spontaneous velocity,

$$\mathbf{D}_{sp} = -\frac{\nabla\tau_c}{|\nabla\tau_c|^2}, \tag{11}$$

in the direction of the gradient of the induction time. This is true when D_{sp} is the fastest speed of the propagation of the reaction. For the deflagration and detonation modes of burning, the propagation speed is limited from above by D_{CJ}. On the other hand, the speed of the spontaneous wave can only be limited from below by the laminar flame speed, or, if detonations are present, by D_{CJ}. For example, D_{sp} is infinite for a uniform distribution of τ_c that corresponds to instantaneous burning at constant volume. More detailed discussion of Eq. (11) can be found in [94, p. 294].

Consider the case for which D_{sp} is finite but greater than D_{CJ}. To be specific, consider a two-dimensional elliptical temperature distribution,

$$T = \max\left(\left(1 - \frac{\sqrt{x^2 + (y/a)^2}}{\mathcal{L}}\right)T_{max}, T_{min}\right), \quad (12)$$

where $\mathcal{L}$ is the characteristic scale of the temperature gradient. For $a = 1$, the distribution becomes cylindrically symmetric. The temperature decreases outward until it reaches T_{min} and then stays constant. From Eqs. (11) and (12), we can obtain a temperature gradient with the components

$$\nabla T = \frac{T_{max}}{\sqrt{x^2 + (y/a)^2}\mathcal{L}}\left(x, \frac{y}{a^2}\right) \quad (13)$$

and the absolute value of the spontaneous velocity

$$\begin{aligned} D_{sp} &= \left(\frac{\partial \tau_c}{\partial T}\right)^{-1} \frac{1}{|\nabla T|} \\ &= \left(\frac{\partial \tau_c}{\partial T}\right)^{-1} \left(\frac{T_{max}}{\mathcal{L}}\right)\sqrt{\frac{x^2 + (y/a^2)^2}{x^2 + (y/a)^2}}. \end{aligned} \quad (14)$$

The temperature distribution described by Eq. (12) for $T_{max} = 800$ K, $T_{min} = 600$ K, $\mathcal{L} = 1$ cm, and $a = 3/2$ is shown in Fig. 22a. This structure, based on the predetonation condition in Fig. 7, is taken as the initial conditions for a simulation of the evolution of an isolated hot spot. The chemical model and numerical algorithms are the same that produced the results shown in Fig. 7. Fig. 22b uses the density distribution at selected times during the explosion to illustrate the evolution of the system. The superimposed contour $D_{sp} = D_{CJ}$ is elongated in the y-direction. Inside this contour, a spontaneous wave propagating with a speed $D_{sp} > D_{CJ}$ is possible. We call this the "spontaneous region." The reaction in this region will spread from the point of minimum τ_c with the speed predefined by Eq. (14).

At 2.776 ms from the beginning of the simulation, the spontaneous wave is inside the spontaneous region. There is no shock wave present, and the distribution of density is continuous. The shape of the spontaneous wave is elongated toward the y-direction, and the overpressure is higher in the x-direction where D_{sp} is lower. At 3.156 ms, the spontaneous wave has almost reached the boundary of the spontaneous region in the x-direction. In both frames, the shape of the spontaneous wave is elliptical with the aspect ratio $\simeq$1:3.

By 3.216 ms, the spontaneous wave has partly exited the spontaneous region. A weak shock wave has been formed and is present within the part of the reaction wave located outside the spontaneous region. There is no shock present in the part of the wave that is inside. The next two frames, 3.395 and 3.792 ms, show the further evolution of the reaction wave with the shock wave developing outside the spontaneous region and growing in strength continuously. The boundary separating the parts of the wave with and without the shock follows the contour of constant $D_{sp} = D_{CJ}$. In the last frame, the wave exited the spontaneous region completely and developed a shock discontinuity in all locations.

Fig. 23 shows the density and pressure profiles at different times along three lines, all with the origin at $x = y = 0$, and then going along the x-axis, the y-axis, and the 45° diagonal direction. Along the x-direction, (Fig. 22a) profile *2* shows the smooth structure of the spontaneous wave without a shock. The material is being continuously compressed while it burns and reaches maximum compression when the fuel is burnt completely. Then the material begins to expand and decelerate. The shock emerges between the times corresponding to profiles *3* and *4*. Profile *4* shows the structure of the wave that is intermediate between the spontaneous wave and a detonation. The material is first compressed continuously, and only then passes through the shock. Profile *6* shows the developed detonation wave.

The same process takes place in the diagonal and y-directions, but with different timings. The latest profile, *6*, corresponds to the time in between the fourth and fifth frames in Fig. 22b. At this time, the wave in the y-direction (Fig. 23c) has not exited yet from the spontaneous region and has not yet developed a shock discontinuity. The wave in the diagonal direction shows that a shock has formed. The overall picture of the explosion of the hot spot obtained in the numerical simulation is fully consistent with the theoretical analysis presented [6].

The same mechanism for triggering a detonation was found in all of the DDT simulations we performed. The detonation always developed through the gradient mechanism from a hot spot that appeared somewhere in the vicinity of the turbulent flame. This mechanism was suggested by theoretical analyses and confirmed by the numerical simulations. The spontaneous reaction waves that we observed are supersonic reaction waves in which burning material is compressed and accelerated in the direction of the wave propagation. The spontaneous waves that lead to detonations initially propagate with the velocity $D_{sp} > D_{CJ}$. When D_{sp} approaches D_{CJ}, a shock front develops inside the reaction zone. After that, the internal structure of a spontaneous wave transforms smoothly to that of a detonation through the series of intermediate regimes with increasing strength of the shock, which eventually moves ahead of the reaction zone.

Many past analyses [30,32,54,55,57,58,60–62] have shown that there are also critical conditions for the gradient of τ_c and the size of the hot spot. If

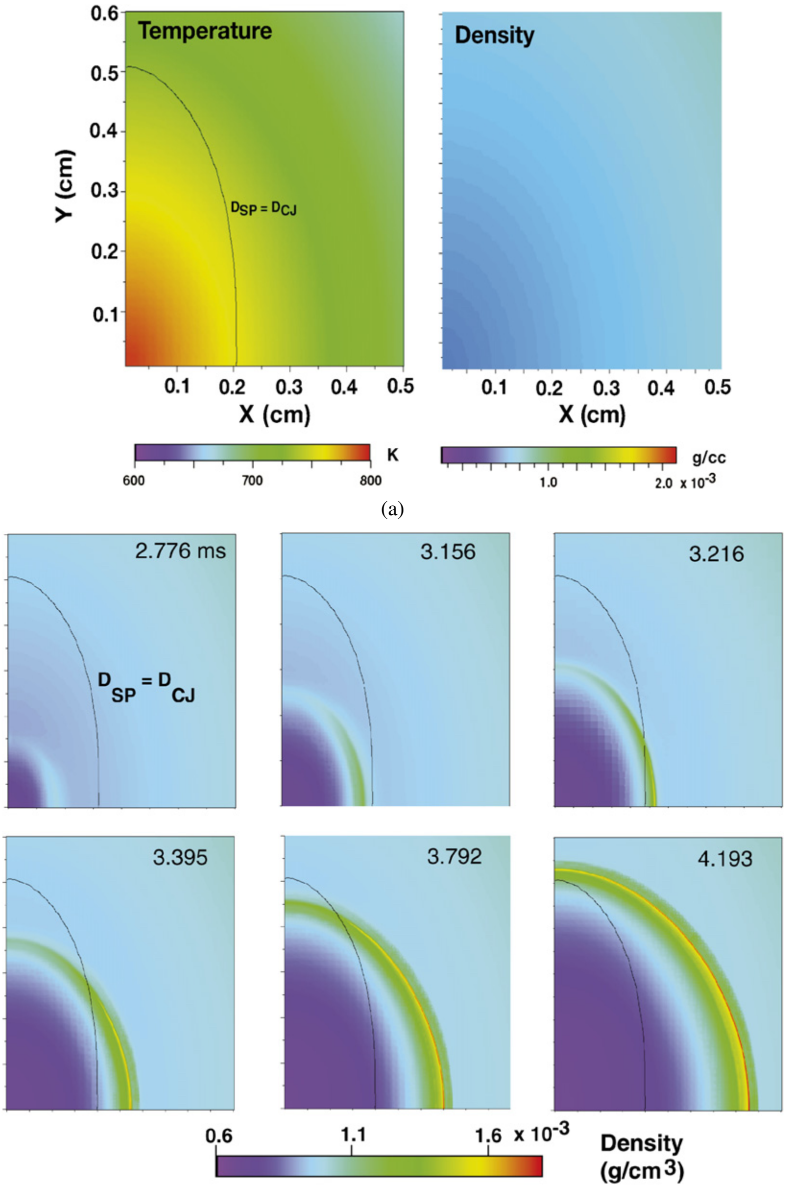

(a)

(b)

Fig. 22. Initial conditions and evolution of a hot spot [6]. (a) Initial temperature and density distributions in an initially isobaric hot spot described by Eq. (12) with $T_{\max} = 800$ K, $T_{\min} = 600$ K, $\mathcal{L} = 1$ cm, and $a = 3/2$. The contour $D_{\mathrm{sp}} = D_{\mathrm{CJ}}$ shows the boundary of the spontaneous region. (b) Density distribution at different times during the explosion of hot spot described by (a). Contour $D_{\mathrm{sp}} = D_{\mathrm{CJ}}$ shows the boundary of the spontaneous region.

the distribution of τ_{c} does not meet these conditions, the detonation does not develop, and the spontaneous wave degenerates into a shock and a residual flame. We routinely observe these failed DDT phenomena in simulations. For example, there are two hot spots in Fig. 3 discussed earlier in this paper. The spontaneous wave velocity computed for the hot spot on the right side is below $0.5 D_{\mathrm{CJ}}$ everywhere [3]. This hot spot produced a shock and a flame behind it because the spontaneous wave was too weak to become a detonation. The shock it created, however, affected the second hot spot, which met the critical conditions for successful transition to detonation.

9. Formation of reactivity gradients

According to Dorofeev [32] and Thomas (personal communication), the deflagration-to-detonation tran-

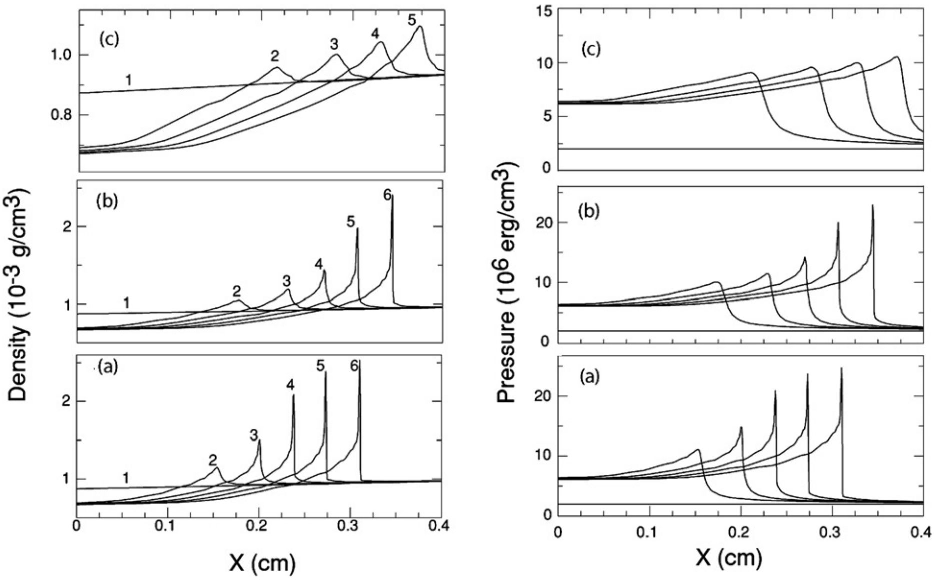

Fig. 23. Density profiles (left) and pressure profiles (right) along three different lines passing through the center of the hot spot at various times during the hot spot explosion [6]. (a) Along the X-axis; (b) along the diagonal; and (c) along the Y-axis. Times are (1) 0 µs; (2) 2.776 µs; (3) 3.016 µs; (4) 3.213 µs; (5) 3.395 µs; (6) 3.587 µs since the beginning of the simulation.

sition has two separate stages: (1) the creation of conditions for the onset of detonation, and (2) the actual formation of the detonation wave itself. The mechanism for the detonation wave formation, given the appropriate background conditions, seems to be universal and involves reactivity gradients. The creation of the background conditions, however, can occur in many ways.

Gradients of reactivity or induction time are usually related to temperature and concentration gradients. These can be created by a variety of different processes that could involve heat conduction, mass diffusion, viscous friction, adiabatic compression, and electromagnetic radiation. For example, consider an idealized one-dimensional test problem in which there is a temperature gradient in the vicinity of a hot wall. If the wall temperature is constant, the material will eventually ignite at some distance from the wall, and a spontaneous reaction wave will propagate toward and away from the wall. Another one-dimensional example is the material compressed by a planar shock. In this case, the induction-time gradient appears because the material behind the shock is compressed at different times depending on the distance from the shock. The induction time first expires far from the shock, then a little closer to the shock, then even closer, etc., so the spontaneous reaction wave propagates toward the shock. This wave can undergo transition to a detonation before it reaches the original shock, or produce a flame and a decoupled shock.

A detailed study of mechanisms of detonation formation due to a temperature gradient, including an asymptotic analysis and numerical simulations, is presented by Kapila et al. [58]. Bartenev and Gelfand [95] also consider the mechanisms of spontaneous initiation of detonations and give an overview of experimental methods for creating induction-time gradients. In the calculations described in previous sections of this paper, the hot spots, which were themselves gradients in reactivity, resulted from effects of shock–flame interactions on the background unburned material. Now we discuss some other scenarios leading to gradients in reactivity and spontaneous waves.

9.1. Shock-induced ignition

The two limits of shock-induced ignition of homogeneous exothermic mixtures are often called strong and weak (or mild) ignition [96–98]. Strong ignition results in a detonation that either is directly initiated by a strong shock or originates from a planar spontaneous wave that forms behind a strong shock. Idealized one-dimensional ignition scenarios rarely occur in real systems. Even for a homogeneous mixture compressed by a planar shock, a smooth, one-dimensional gradient of induction time can be perturbed by multidimensional local fluctuations of density, temperature, and concentration. As a result, the induction time will first expire in one or more hot spots, energy release will begin, and spontaneous waves will propagate from these points.

The role of fluctuations and the multidimensional nature of ignition become more obvious for weaker shocks that produce gentler gradients of induction

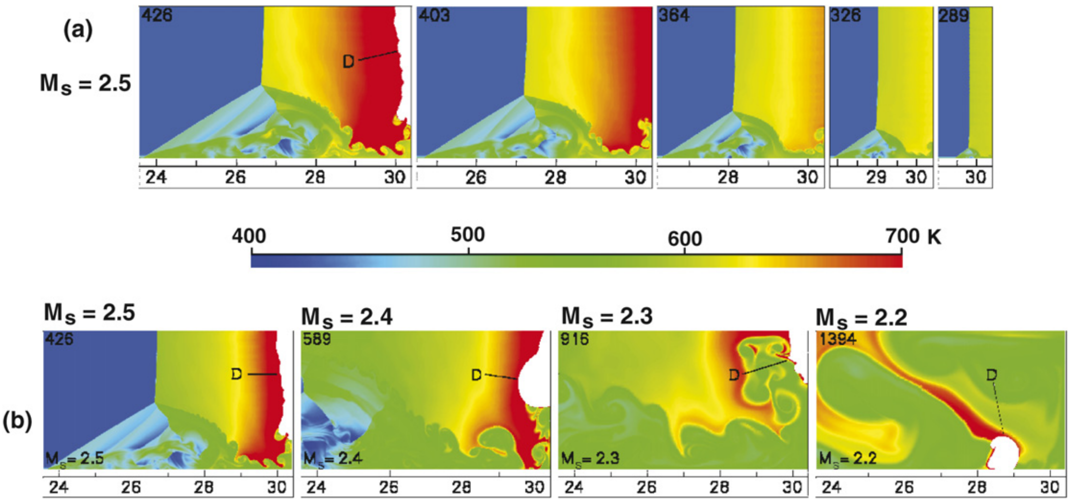

Fig. 24. (a) Sequence of temperature fields showing the evolution of the reflected shock interacting with a boundary layer in a stoichiometric ethylene–air mixture for $M_S = 2.5$ and $d/2 = 3.8$ cm [8,13,14]. Time (μs) is given on the upper left side in each frame. Length scale is in centimeters. (b) Temperature fields shortly after ignition for $d/2 = 3.8$ cm and four different values of M_S [8,13,14]. Time (μs) is given on the left side of each frame. Length scale is in centimeters. White areas contain burned material with temperature about 3000 K; D indicates detonation.

time in shock-compressed material. In this case, small changes in induction time due to local fluctuations can significantly affect the locations of initial thermal explosions. The resulting weak ignition is characterized by the appearance of a number of small flames followed by a transition to a detonation. Shock-induced ignition is further complicated by walls and boundary layers [8,13,14] that are always present and are a major cause of the nonuniform flow observed in experiments with reflected shocks.

Consider the computational setup shown in Fig. 10, but now with no flames present: there is a channel filled with a stoichiometric ethylene–air mixture defined in Table 3 and a shock with Mach number M_S entering the channel from the left. Again, we model the lower half of a channel using the symmetry conditions at the upper boundary and no-slip wall conditions at the bottom and right walls. A series of simulations was performed for this system for a range of M_S and channel widths. For $M_S = 2.5$, the incident shock is too weak to induce any significant energy release before it reaches the end wall. The reflected shock, however, is strong enough to start the energy release, which quickly increases the temperature near the end wall, as shown in Fig. 24a for $d/2 = 3.8$ cm. The temperature distribution is not quite uniform because of the shock bifurcation and the relatively cold wall jet that removes the hot material from the region around the lower corner near the end wall. Since most of the channel width is unaffected by the wall jet, there is a series of thermal explosions occurring almost simultaneously along the end wall surface. The resulting shock wave is strong enough to trigger a detonation D that subsequently overtakes the reflected shock. This is a typical case of strong ignition just slightly disrupted by boundary-layer effects.

For weaker shocks, the temperature behind the reflected shock is lower, and the chemical induction time increases. This allows the bifurcated structure to grow before ignition occurs. The wall jet has more time to transport cold material towards the end wall, and this further disrupts ignition. Temperature fields shortly after ignition for $M_S = 2.5$, 2.4, 2.3, and 2.2 are shown in Fig. 24b. The surface area at the end wall where the explosion occurs decreases systematically with M_S. For the lowest value, $M_S = 2.2$, the wall jet has enough time to remove all of the hot material from the surface of the end wall, and an explosion occurs away from the wall. These results are consistent with experimental observations [98] of autoignition of hydrocarbon–oxygen mixtures diluted with argon behind bifurcated reflected shocks.

For similar flows in narrower channels, the effects of boundary layers become more important. Fig. 25 shows a sequence of temperature fields for $M_S = 2.4$ and $d/2 = 0.95$ cm. Here the wall jet removes hot material from the entire surface of the end wall and thus prevents the mixture from igniting at the reflecting wall. There is, however, another route to ignition. The bifurcated foot grows quickly, reaches the center of the channel (top symmetry plane of the computational domain), and creates several secondary shocks. Reflections of these shocks and their interactions with vortices intensify mixing in the shock-compressed

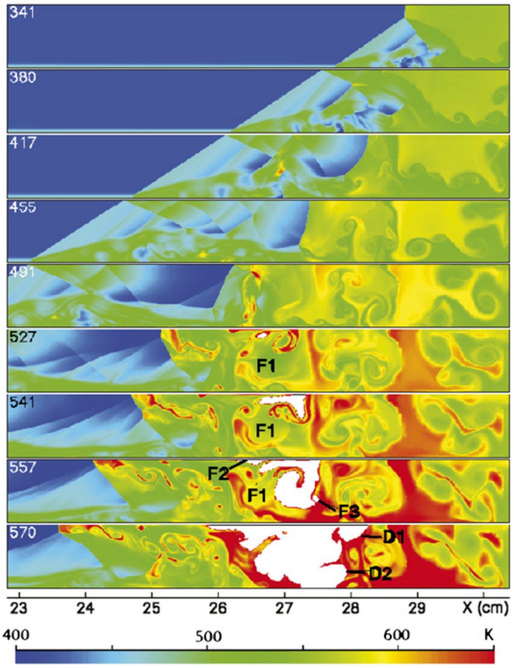

Fig. 25. Sequence of temperature fields showing the evolution of the reflected shock interacting with a boundary layer in a stoichiometric ethylene–air mixture for $M_S = 2.4$ and $d/2 = 0.95$ cm [8,13,14]. White areas in the last four frames contain burned material with temperature about 3000 K. The letters indicate flames (F1, F2, F3) and detonations (D1, D2). Time (μs) is given on the left side of each frame.

material and create hot spots. Most of these hot spots disappear because of interactions with vortices and rarefaction waves. One of the hot spots survives long enough to produce a flame F1. The flame develops and interacts with vortical structures, and generates weak compression waves that heat the surrounding material. This process creates more hot spots. Two hot spots produced flames F2 and F3, and two others eventually lead to detonations D1 and D2. This sequence of ignition events occurring behind a reflected shock, away from the reflecting wall, is a typical case of weak ignition.

9.2. *Laminar flames*

For some reactive systems, an induction-time gradient necessary for DDT can be created by a laminar flame. Consider the case in which two flame surfaces approach each other. This may occur when the flame surface is distorted because of flame instabilities or flame–flow interactions, or there are two different, unconnected flames. When the thickness of the layer of unreacted (or partially reacted) material between the flames becomes comparable to the flame thickness, the temperature of the layer increases due to the heat transfer from the reaction zone. If the flame surfaces are not exactly parallel to each other, the temperature increase is not uniform and produces a temperature gradient along the layer. Eventually, the reaction starts at some point in the layer. As a result, the flames merge at this point and a spontaneous wave begins to propagate along the unreacted layer away from the merging point. The temperature gradient in the layer and the spontaneous wave velocity depend on the angle between the flame surfaces. The spontaneous wave can become a detonation if the gradient profile is appropriate.

We have observed this DDT process in numerical simulations for a model system with a very high thermal conductivity that resulted in very fast, thick flames [8]. Fig. 26 shows a simulation of a laminar flame approaching the bottom boundary. There is a symmetry plane at the bottom, so that there is, in effect, another flame below the computational domain. As the flames collide, a spontaneous wave appears at 139 μs near the collision point, propagates through the reactivity gradient in unreacted material between flames, and generates a shock. The central part of this shock propagates with the spontaneous wave along the unreacted layer. Other parts of this shock interact with the reacting material in the flame thus accelerating the energy release, and spread into the burned material behind the flame surface. Because shocks propagate faster in the hot burned material surrounding the unreacted layer, they are able to overcome the central part of the shock and modify the temperature gradient in the unreacted layer ahead of the spontaneous wave. These multidimensional effects help to synchronize the shock compression and the energy release and thus contribute to the development of a detonation wave that appears at 215 μs. Similar phenomena resulting from Darrieus–Landau instabilities were observed in simulations [99] that modeled systems with a very high laminar flame speeds. It is still unclear if this mechanism can be realized in practical combustible systems.

9.3. *Turbulent flames and unconfined DDT*

An induction-time gradient can also be created by mixing hot burning products and fuel [43]. This describes one scenario that fits into the last category of experiments used to study DDT, as mentioned in the Introduction and described in Section 3. This situation could occur when high-intensity turbulence locally extinguishes the flame [61].

In early work, we presented a substantially theoretical argument for the possible occurrence of unconfined DDT based on the effects of background turbulence on an existing flame [61]. The fundamental mechanism considered was this: background turbu-

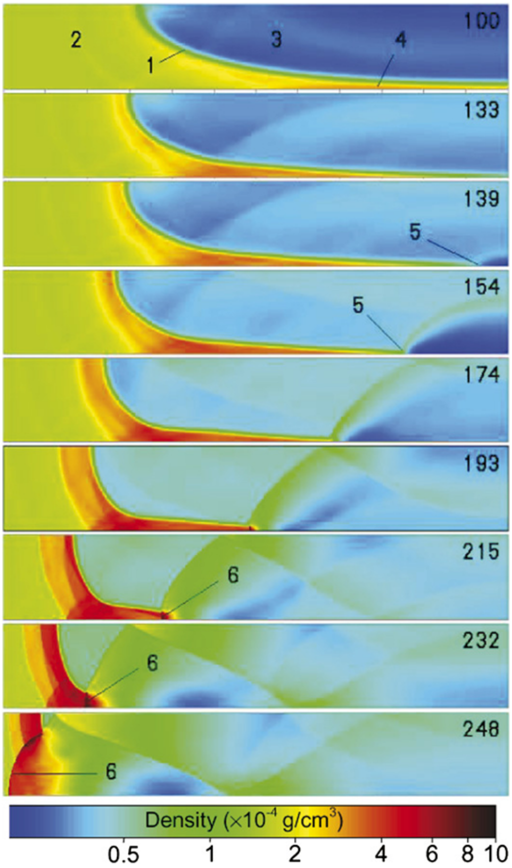

Fig. 26. Spontaneous wave and detonation emerging in a model system that contains only a laminar flame [8]. Flame surface **1** (top frame) separates premixed unreacted material **2** (green) from burned products **3**. Temperature gradient forms in the unreacted layer **4** near the bottom boundary (symmetry plane) when the flame surface approaches it. Spontaneous wave **5** propagates through this gradient and forms detonation wave **6**. Time (μs) is given on the right side of each frame. The reactive system parameters correspond to the stoichiometric ethylene–air mixture described in Table 3, except for the thermal conductivity, which was increased by a factor of 100. Top, bottom, and right boundaries are symmetry planes; left boundary is open.

lence extinguishes the turbulent flame and mixes hot products with cold reactants. This mixed region forms an induction time gradient that could undergo a transition. Then an analysis of the level of turbulence required to extinguish the flame gives an estimate of the background turbulence required for unconfined DDT. There are two key elements to this theory:

1. *The size of the hot spot, characterized by a gradient in a region of length L_d that can trigger DDT in a mixture of hot burning products and fuel.*
   A series of one-dimensional simulations of detonations developing inside a mixed region [61] lead to the estimate $L_d \sim 10^3 x_d$, where x_d is the thickness of the one-dimensional reaction zone of the CJ detonation, or $L_d \simeq 36 l_c$, where l_c is the detonation cell size, or $L_d \sim 10^4 x_l$, where x_l is the laminar flame thickness. This estimate of the critical size of the mixed region is roughly in agreement with the results of hot jet initiation experiments and implies that large-scale mixing is required to precondition the region.
2. *The intensity of turbulent motions required for the region of size L_d to undergo DDT.*
   For the turbulence to be able to extinguish the flame inside the region of size L_d, the Gibson scale λ_G [100] inside this region should be comparable to or less than the thickness of the laminar flame x_l.

For Kolmogorov turbulence, the Gibson scale can be computed as

$$\lambda_G \simeq \left(\frac{S_l}{U_L}\right)^3 L, \tag{15}$$

where S_l is the laminar flame speed, L is the driving scale of the turbulence, and U_L is the turbulent velocity on this scale. If $\lambda_G = x_l$, then

$$U_L = K S_l \left(\frac{L}{x_l}\right)^{1/3}, \tag{16}$$

where K is a coefficient introduced to describe the ability of the flame to survive stretching and folding caused by turbulence on the scales of order x_l. Once the condition of Eq. (16) is reached for a large enough region ($L \geqslant L_d$), detonation can develop through the gradient mechanism. This requires the speed of the turbulent flame brush to be $\sim 10^2$ times faster than the laminar flame speed [61]. The high turbulent velocity required in the background material means that unconfined DDT is extremely difficult to achieve by turbulence generated by the flame itself or by the Rayleigh–Taylor instability. This helps to explain why DDT in unconfined flames is so hard to observe.

This theory was also used to explore possibilities for DDT in thermonuclear supernovae [101]. It can also be extended to confined DDT in the cases when the explosion leading to detonation takes place in the middle of a turbulent flame brush. Flame-extinguishing phenomena considered by this theory are difficult to reproduce in numerical simulations due to the wide range of spatial scales involved and the intrinsically 3D nature of turbulent flames. Successful numerical simulations of unconfined DDT are still to be done.

10. Open questions and future research

The simulations described here have brought up a number of issues and questions that need further investigation. For example, what is the nature of the turbulence in highly compressible, dynamic reactive flows? How sensitive are the simulations to small changes in parameters? How do better chemical models change the results? How do better or even different numerical algorithms affect the answers? How does the size of the system affect the likelihood of DDT? Can there really be a truly unconfined detonation? Below we summarize what we know about some of these interesting, open questions.

10.1. Nonequilibrium turbulence

The observed trends in when and where DDT occurs in the simulations agreed reasonably well with results of shock-tube experiments. For example, as M_S increased, hot spots appeared more often and closer to the flame front. When the flame was ignited and remained far from the wall, so that it could not interact directly with the bifurcated structure, no supersonic flame formed. When the flame was closer to the wall as the shock passed, a strange wave formed after shock reflection. All of this is understandable and encouraging. There was, however, an additional nagging concern because we did not expect the values of M_S for the occurrence of DDT in two-dimensional systems to be so close to those in the experiments. We also did not expect the values of more global properties, such as the time to formation of the first hot spot, to be so similar in two- and three-dimensional calculations. One explanation for this could be the unusual type of turbulence generated in this system by repeated shock–flame interactions. Here we examine this is slightly more detail.

The origin of the turbulence in the initially laminar flame was *not* the relatively slow, natural flame instabilities usually studied for laminar flames, but Richtmyer–Meshkov instabilities induced by repeated shock–flame interactions. These start on the largest scale with the first interaction of the laminar flame with a shock. The first interaction has a relatively mild effect on the increase in the burning rate [1], but it sets the stage for the effects of subsequent interactions. After this, the already convoluted flame is shocked repeatedly. Because of this frequent, continual shocking, vorticity is generated on a range of scales simultaneously, from the scale of the system to the smallest scale of the flame thickness, in both the two-dimensional and three-dimensional calculations. This is independent of and can be much more effective in populating different scales than the energy cascade. Another source of turbulence on small scales is the Kelvin–Helmholtz instability on these scales, but it also appears to be less important than the RM instabilities for the flows under consideration.

The behavior of the RM instability in two and three dimensions has been studied by many authors in a number of different scientific communities. (There is a recent review by Brouillette [66].) The results most relevant to our arguments here are the theoretical analyses and numerical simulations of the RM instability for the Euler problem by Li and Zhang [65]. These authors compared the two- and three-dimensional growth rates as a function of time for reflected shocks and rarefactions. The results related to both the linear and nonlinear phases of the interaction. First, as long as the initial amplitude and wavelength of the perturbation are the same, the growth rate of the instability in two and three dimensions are essentially the same in the linear regime. Then, in the nonlinear regime, the three-dimensional growth rates are about 20–25% larger and faster, respectively, than for 2D. This is consistent with the type of growth in surface area and energy release computed for the two- and three-dimensional flames [1].

Thus the fact that computations in two dimensions show agreement in trends and behavior with those in three dimensions and with experiments appears to be consistent with the RM instability being the major mechanism for generating the turbulent flame. This is because, as argued above, at least the qualitative behavior of a system dominated by RM should be similar in two and three dimensions. Flow dominated by repeated shock–flame interactions occurring on all scales cannot be expected to have the isotropic, homogeneous, equilibrium spectrum characteristic of the type of turbulence that has been the topic of intense study in the past 30 years. In fact, this kind of flow perhaps cannot even be technically called turbulence. We refer to it as *nonequilibrium turbulence*, or *non-Kolmogorov turbulence*. The properties of this nonequilibrium turbulence and how it decays to the more standard equilibrium state are topics that require considerably more work and are ripe for direct numerical simulation and theoretical analyses.

10.2. Sensitivity and models for large-eddy simulations

There are important, unanswered questions about the sensitivity of the solution to changes in basic material properties and configurations. For example: How do the results change if the Lewis number is changed? If there is a change in the position or shape of the flame? If there are multiple obstacles or multiple, separate flames in the domain? If the material parameters are changed? If the background temperature and pressure are changed?

Any of these questions could be a separate research project that would involve many individual computations to determine and understand trends. As we have learned, the results are not always intuitive. As system properties are changed, previously unimportant effects or even different physical phenomena may develop and change the trends. For example, the development of the strong Mach stem in the bifurcated shock system (Figs. 11b and 14) created higher temperatures and pressures in unreacted gas, and this meant that hot spots were more likely to develop. A wider channel might not show the same events or timings of events. Another example was seen in the shock-tube autoignition simulations (Figs. 24 and 25). The way in which hot spots form and DDT occurs changes as the shock intensity changes. For a strong shock, a relatively uniform gradient in reaction time forms as the shock reflects from the wall and heats and compresses the reactive material. For a weaker shock, the reaction is slower, the material that was heated the longest is diluted with material from the wall jet that is part of the shock bifurcation, and hot spots may simply occur later and in different turbulent regions of the material. These two mechanisms of creating reactivity gradients are quite different.

It has been suggested that the information about how hot spots arise in unreacted material could be the basis for subgrid models for large-eddy simulation in which DDT might occur. The idea would be to resolve events in the large-scale flow and use them to indicate when and how to ignite random detonations. This approach to forming a stochastic subgrid model to predict DDT might work, but only after we understand the overall sensitivity of hot-spot formation to system parameters.

10.3. *Model and method improvements*

Developing the numerical model for the simulations required evaluating trade-offs and making compromises between speed (which would allow us to even contemplate the computations) and accuracy (which would allow them to show anything of interest on DDT). The bottom line was always to use the most efficient numerical methods and the least complicated physical submodels possible to describe the fluid dynamics and combustion processes. There are, then, a number of questions we should address now: Do we need high-order algorithms? What additional or more complex representations of the physical processes must be incorporated? When is there enough resolution, and where do we need it? What are useful tests?

Consider first the issue of the simplicity of the physical submodels. The chemical model in equations solved (Eqs. (1)–(9)) is extremely simple compared to what we are capable of solving for a smaller computational domain. The results produced seemed reasonable for the ethylene and acetylene experiments, but a more complex chemistry may be needed for other reactive systems. We do not know the effects on the solution of using more detailed chemical models or including other processes, such as radiative losses.

There are also issues with the current AMR and its implementation. Using a low-order fluid-dynamics algorithm means living with more global diffusion and a less resolved fluctuation spectrum. But this allowed an efficient parallelization of the algorithm, and therefore we could attempt to compensate with resolution. The problem of accuracy in the fluid algorithm is currently being addressed through the development of a higher-order method, flux-corrected transport, on the FTT [83]. This work has answered some of the fundamental questions of accuracy and monotonicity in terms of wave transmission when neighboring computational cell interfaces vary in size by a factor of 2. There are now efforts to parallelize this so it will be available for large-scale DDT simulations.

10.4. *A continuing quandary: unconfined DDT in Type Ia supernovae?*

The laboratory DDT scenarios described in this paper relied heavily on shocks, shock reflections, and the presence of walls or obstacles, all of which decrease the critical length scale required for DDT to form in a specified material. Actual hazardous situations in chemical plants and storage facilities always involve some confinement. It is harder to see how DDT could occur when there is minimal or no confinement. One example of a situation in which DDT could occur with minimal confinement is in a large vapor-cloud explosion in open space. Even in this case, however, shocks could reflect from airborne particles or debris, large obstacles, or eventually from the ground.

The most extreme case where DDT may occur is in a Type Ia supernova (SNIa), which is completely unconfined (see [20] for a review). White dwarf (WD) stars, which are believed to be the progenitors of SNIa, are composed of a mixture of fully stripped ^{12}C and ^{16}O ions, in about equal proportions, immersed in a degenerate electron gas. Although this material has properties that are far from the normal gases of laboratory experiments or terrestrial explosions, it has many characteristics that make its behavior similar to gas-phase combustion in terrestrial systems. These similarities allow us to define thermonuclear flames and detonations and to treat the supernova explosion as a combustion process. Currently, one of the major unanswered questions about the physics of thermonuclear supernova explosions is related to the topic of this paper: *Does DDT occur in SNIa, and if so, how does it happen?*

The mass of a stable WD is always less than the Chandrasekhar limit, $\simeq 1.4 M_\odot$, where $M_\odot$ is the mass of the Sun. Above this limit, there cannot be hydrostatic equilibrium of degenerate matter with equal numbers of protons and neutrons [102,103]. Though an isolated WD is stable and almost inert, more than 50% of all stars are part of multiple star systems. The dynamics of multiple-star interactions could involve additional mass transfer from one star to another, and thus increase the WD mass until it approached $1.4 M_\odot$. This would make the WD unstable, so that it would ignite and explode. The explosion destroys the star in about 2 s, releasing about 1.5×10^{51} ergs.[2] The energy is produced by the network of thermonuclear reactions that begins with ^{12}C and ^{16}O nuclei and ends in ^{56}Ni and other iron-group elements. Intermediate-mass elements, such as Ne, Mg, Si, S, and Ca, are also created.

The input physics for the model for the SNIa explosion is an equation of state of a compressible degenerate gas, a nuclear reaction network, electron thermal conduction, essentially no molecular diffusion (infinite Lewis number), and strong, spatially varying gravitational forces. The explosion could start at the center of the star as a weak ignition process, in which natural fluctuations in the compressible reactive mixture create a small region of high temperature and accelerated reaction. A priori, the results could be a flame or a detonation: the material, in principle, supports both.

Studies of thermonuclear explosions in WDs have followed a route similar to those in combustion science: As computational resources have increased, problems solved have progressed from one-, to two-, and now to three-dimensional solutions, with increasing complexity in representing contributing physical processes. One-dimensional detonation models of SNIa [104,105] do not reproduce the observed spectra. Both one-dimensional deflagration models [106–108] and delayed-detonation models [109–111] claimed the best fit to observational data. Both types of models, however, contain a number of uncertain parameters, such as the turbulent flame speed and the time for detonation initiation. Two-dimensional SNIa flame simulations show the importance of the gravity-induced Rayleigh–Taylor instability in making the flame turbulent and give some indication of how the large structures formed early in the evolution of the flame can mix core and outlying material in the star. Two-dimensional detonation simulations [112,113] show the importance of multidimensional detonation cell structures and large unburned pockets that may change the distribution of species in the ejecta.

Three-dimensional models for WD explosions must deal with a series of severe computational problems related to the range of physical scales of the flow and the complexity of the reaction mechanism. As discussed in [20], the range of space scales spans 12 orders of magnitude, from the size of the star to the thickness of a thermonuclear laminar flame. This is a case where adaptive mesh refinement helps, but does not completely solve the problem. A full nuclear reaction mechanism (e.g., [114–117]) that extends from carbon and oxygen through to nickel is both extremely large and very stiff to integrate.

Three-dimensional simulations of WD explosions have become possible only recently [17–19,118–120] with advances in computational technology. For example, Fig. 27 shows a sequence of frames from a three-dimensional computation of a deflagration in a WD [17]. Here the flame was propagated using a flame-tracking model that moved the flame front locally according to background conditions and a subgrid model for the turbulent flame speed. The subgrid model was based on the assumption that the turbulent flame development was dominated by the Rayleigh–Taylor instability [17,101,121]. The initial condition is a spherical flame ignited in the center of the WD. This flame initially propagates outward with laminar flame speed $S_\mathrm{l} \sim 10^7$ cm/s. As it moves away from the center, the effects of gravity increase and so does the rate of development of the RT instability. Due to this instability, small perturbations on the flame surface grow and form plumes that have characteristic mushroom shapes. The turbulent flame speed S_t increases with gravity and eventually dominates S_l. The flame plumes continue to grow, due partially to the flame propagation and partially to gravitational forces that cause the hot, burned, low-density material inside the plumes to rise toward the WD surface. Gravity also pulls the cold, high-density, unburned material down between the plumes toward the center. Shear flows along the flame surface are Kelvin–Helmholtz (KH) unstable and quickly develop vortices, which continue to distort the flame surface and create smaller-scale turbulent motions. The turbulence in SNIa is driven by RT instabilities, in the same way that the turbulence in the laboratory experiments was driven by the RM instabilities. The nature and nonequilibrium properties of this turbulence is also a topic of future research.

When the original flame plumes grow large enough, secondary RT instabilities eventually develop on the surface of the first mushrooms, and these, in turn, can develop instabilities on their surfaces. This

---

[2] In astrophysics, the units used are cgs and energy is expressed in ergs.

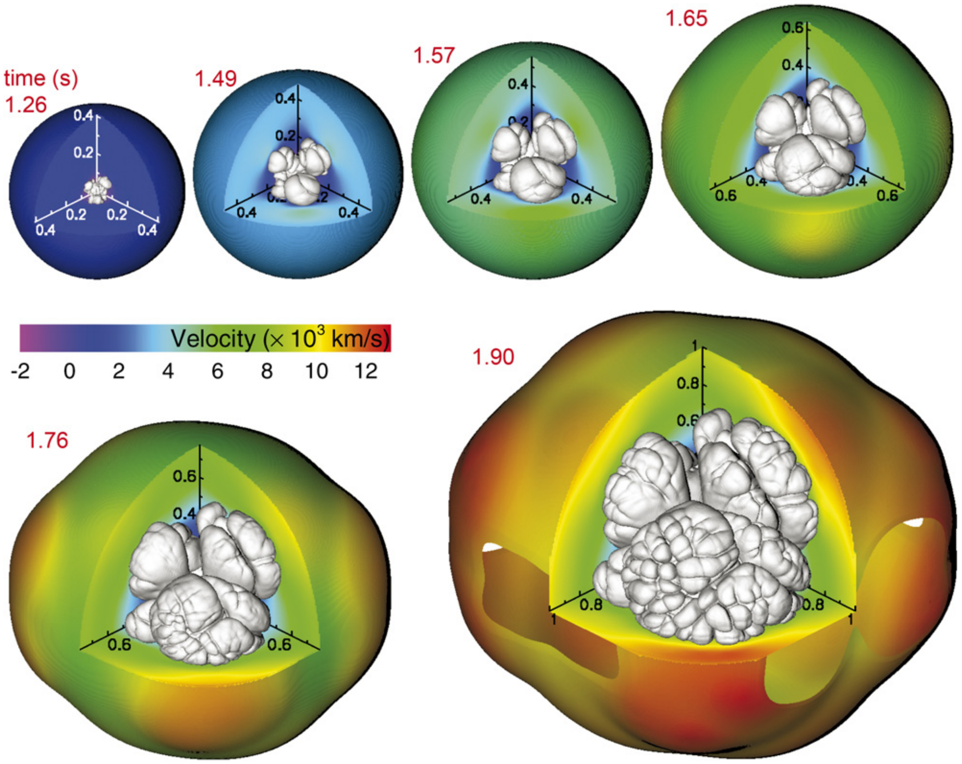

Fig. 27. Development of thermonuclear deflagration in a carbon–oxygen white dwarf star [17]. The gray surface shows the turbulent thermonuclear flame. The color scale shows the radial velocity of unburned material. Distances are scaled by the computational domain size $x_{\max} = 5.35 \times 10^8$ cm. The last frame shows the star surface shortly after it reached the computational domain boundary.

process continues to smaller and smaller scales, resulting in the extremely complicated turbulent flame surface shown in Fig. 27. As the turbulent flame develops, the energy released drives pressure waves outward, causing the WD to expand. The calculation shows that the final value of the energy released, $\simeq 0.6 \times 10^{51}$ ergs, is too low compared to observations, and the resulting composition and distribution of elements do not agree with spectral data. A key feature of the simulations is the highly convoluted turbulent flame surface, which allows extensive interpenetration of burned and unburned materials and leaves unburned carbon and oxygen and intermediate-mass elements in central parts of the WD.

The presence of unburned carbon and oxygen and intermediate-mass elements in central parts of the exploded WD is *not* consistent with observations, which indicates that deflagrations alone do not explain the SNIa explosion. This inconsistency can be resolved if we assume that, at some point, the system undergoes a transition to a detonation. DDT, however, involves hot spots arising at relatively small scales that are not resolved in this simulation. We can study the effects that DDT would produce on the large, resolved scales by assuming a time and a location for the detonation initiation. Fig. 28 shows results from two calculations in which we artificially inserted a hot spot to start a detonation. The deflagration was ignited at the center of the WD, and then a detonation was initiated at either 1.51 or 1.62 s after the beginning of the deflagration. The detonation transforms all carbon and oxygen in central parts of the WD into iron-group elements and produces intermediate-mass elements (rather than unburned carbon and oxygen) in outer layers. This drastically changes the distribution of nuclei compared to that produced by the pure deflagration. The total energy released by this explosion is $(1.3–1.6) \times 10^{51}$ ergs, which is in agreement with the typical range $(1–1.5) \times 10^{51}$ ergs obtained from SNIa observations. Of these two calculations, the earlier detonation ignition produces the more homogeneous results at the end of the calculation, and this is thought to be in better agreement with the symmetry of the observations.

Thus we now have a possible scenario for SNIa, involving DDT, that has at least passed the first tests. We have not yet shown it is correct, which could only be done if we could prove that the conditions leading

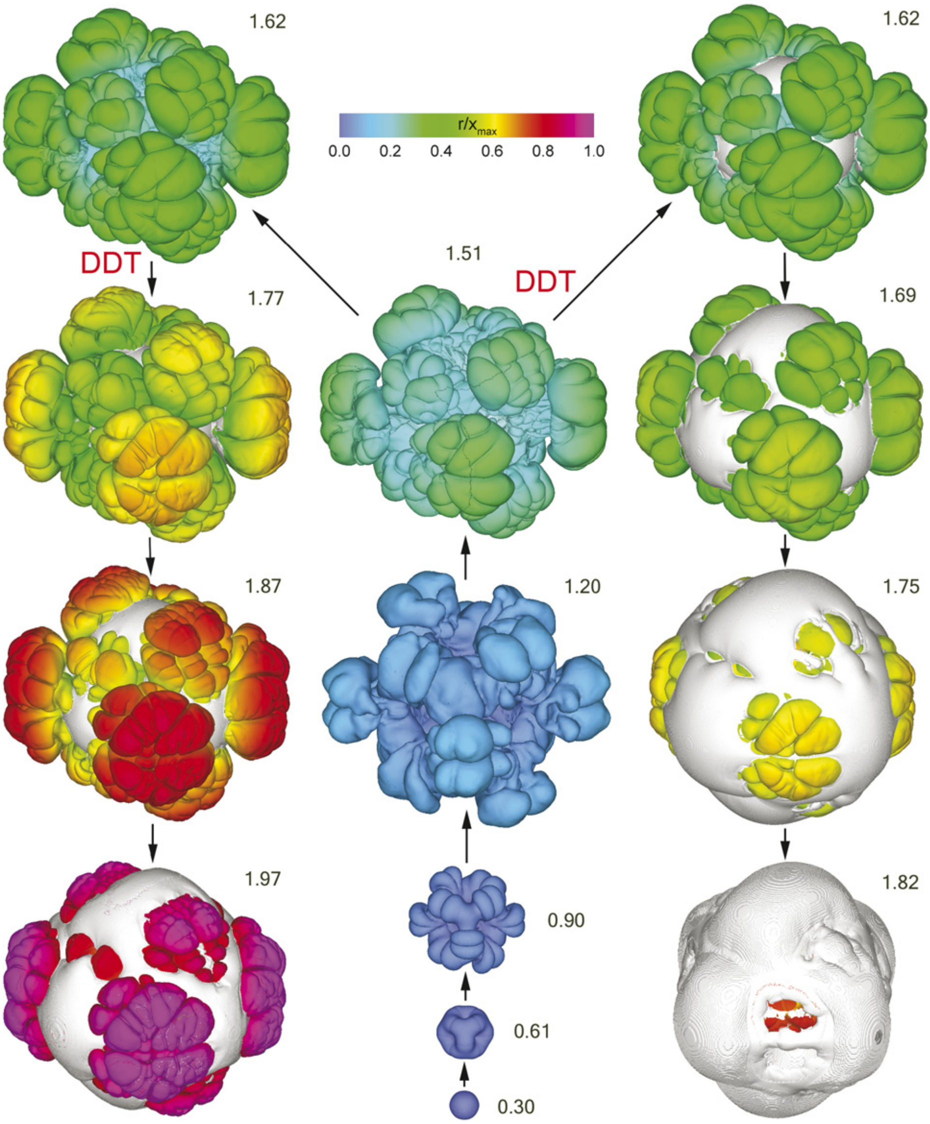

Fig. 28. Development of a turbulent thermonuclear flame (colored surface) and a detonation (gray surface) in a carbon–oxygen white dwarf star [18,19]. Numbers show time in seconds after ignition. Central column shows the deflagration stage. Left and right columns correspond to two delayed detonation cases with the detonation starting at 1.62 and 1.51 s, respectively. Flames at 0.30, 0.61, 0.90, and 1.20 s are plotted at the same scale. Further flame growth is shown by the color scale, which changes with distance from the flame surface to the WD center, $x_{\max} = 5.35 \times 10^8$ cm.

to DDT do occur in the RT funnels. That is the subject of future work.

11. Observations and conclusions

Interactions of shocks and flames are important in creating the conditions under which DDT can occur. Flames generate shocks, especially in confined spaces and in the presence of obstacles, and enhance the strength of shocks passing through a turbulent flame brush. In turn, shock interactions with flames create and drive the turbulence in flames far more dynamically than standard combustion instabilities. Enhanced turbulence means a higher energy-release rate and more fluctuations in background material, which promote hot-spot formation.

Detonations appear when local conditions in unreacted material allow a spontaneous wave to form, and this wave evolves into a shock that is strong enough to become a detonation that can propagate outside the gradient. In a static situation, that is, for isolated hot-spot ignition, these conditions are determined by the gradient in reactivity inside the hot spot. If the hot spot is too small, or the gradient is too gentle or too steep, a spontaneous wave may still form, but it will not lead to a detonation.

In complex, dynamic flows, hot spots could form with almost any geometrical shape. For example, imagine a long thin irregularly shaped hot spot. In this case, the detonation emerges first in the direction where the gradient is most favorable, and later in other directions. Hot spots can, however, arise in very dynamic situations where the temperature gradients inside hot spots are disturbed by shocks or rarefactions passing through them during the ignition process. In that case, the static model still gives some indication of the conditions required for a detonation to develop. There has been significant prior work on the gradient mechanism for creating spontaneous waves leading to detonations, and all of that is directly relevant to the small hot spots we observe undergoing transition to a detonation. For some of these hot spots, the temperature distribution does not allow a detonation to develop, and the spontaneous wave produces a decoupled shock and a flame. This decoupled shock can further affect nearby developing hot spots and eventually help to create a reactivity gradient that will produce a detonation.

In confined DDT problems, the Richtmyer–Meshkov instability resulting from repeated shock–flame interactions is a primary mechanism for generating turbulence in the flame brush that eventually leads to DDT. This mechanism populates all scales, from the flame thickness to the system size, and produces nonequilibrium turbulent spectra. In the early stages, spectra generated by RM instabilities are very similar in two and three dimensions, a similarity we do not see in equilibrium turbulence described by a Kolmogorov model. In the later stages, as shocks die out, this nonequilibrium turbulence should decay to standard Kolmogorov cascade. This is an important topic for further investigation.

The simulations of laboratory experiments described in this paper focused on the first two steps of DDT: (1) how hot spots are formed in an environment affected by a turbulent flame and (2) how a hot spot can support a spontaneous reaction wave, and if such a wave can undergo a successful transition to detonation. But from a practical point of view, there is a third stage (3): Even if a detonation wave forms from a hot spot, larger-scale conditions may not allow it to survive. On the largest scale, there could be geometrical features of the enclosure that suppress the detonation. In our current simulations of DDT in obstructed channels filled with a hydrogen–air mixture [16], we observe detonations that emerge from hot spots, but are unable to spread past obstacles. There has also been extensive work that has given estimates of and provided criteria for determining if a detonation will survive as it passes to larger and smaller channels and diffracts around corners and obstacles. These criteria assume that there is a self-sustained detonation with a developed cell structure and use the detonation cell size as a natural scale.

As discussed in Sections 3 and 9, shock–flame interactions are only one way to create the gradients of reactivity from which spontaneous waves develop. They can also be created by a variety of physical processes involving compression or different forms of transport of mass, momentum, or energy. Several have been described, including weak and strong ignition induced by shock reflection, flame–flame interactions, and turbulent mixing of reactants and products. Weak and strong ignition and turbulent mixing have been the subject of extensive experimental work and some theoretical analysis and simulation. It is not yet clear whether flame–flame interactions can lead to DDT in any realistic situations.

An important issue for DDT simulations is determining how to deal with large disparities in spatial and temporal scales. As described above, spatial scales vary by from 6 to 12 orders of magnitude, and chemical reaction mechanisms should be much more detailed than the single-step mechanism we used. We expect computers to catch up with this problem eventually, but how do we solve practical safety problems for which we need the answers now? How do we continue to make progress in the Type Ia supernova problem? One way is to approach the problem from both ends. In the case of the SNIa, we can simulate the largest scales and attempt to describe the unresolved small scales with subgrid models. We can also study small-scale events separately using high-resolution simulations of a small fragment of the star and use these results to explore the types of conditions that can arise. The same approach extends to DDT problems in practical scenarios, such as hydrogen fuel stations, where there is a danger of ignition and DDT.

Adaptive mesh refinement based on the fully threaded tree that was used in all simulations described here accelerated calculations significantly and so was of major importance in defeating the 1000-year prediction discussed in the Introduction. One problem that arises when using AMR is related to the selection of criteria for increasing or decreasing resolution and the possibility of not resolving or even filtering or diffusing important information. In early two- and three-dimensional simulations of shock–flame interactions in channels with no-slip walls, shock bifurcations at the walls were not particularly evident because boundary layers were inadequately resolved. When tangential-velocity gradients were used as criteria for increasing resolution, boundary layers were resolved and we were able to see shock bifurcation phenomena. An interesting and potentially important question concerns using coarse gridding in flow regions where there is not much activity (such as cold, unreacting flow, which provides little information about the solution), but through which information must be transmitted. Coarse grids could result in filtering important information. A systematic study should be done to determine whether this issue is important for turbulent reactive flows.

The study of DDT described in this paper is an example of cross-disciplinary research. What was learned from studying laboratory DDT experiments has had direct impact on interpreting astrophysical phenomena [122], and what was learned from attempting to model Type Ia supernovae [20] has had direct impact on our understanding and now prediction of practical DDT scenarios. The numerical methods developed during this study have had, and will continue to have, direct impact on terrestrial and astrophysical combustion modeling and other areas of research and engineering applications.

Finally, this work resulted from a serendipitously fruitful collaboration between traditional combustion sciences, astrophysics, and computer science. It was aided by an explosion in readily available computational resources. Fewer, but still significant results could have been obtained with a stagnant computing power, but nothing of what was done would have been possible without the collaborations and the infrastructure that allowed the collaboration. From a scientific sociological point of view, it is probably important to understand how this happened, but that topic is far beyond the scope of this paper.

Acknowledgments

This work was sponsored by the Office of Naval Research and the NASA Astrophysical Theory Program. The bulk of this work was done in collaboration with Alexei M. Khokhlov. We are grateful to Jay Boris for his constant encouragement and suggestions. The authors are very grateful to J. Craig Wheeler and Geraint O. Thomas, who also played major roles in this collaboration. In addition, we thank John C. Clarke, Caren Brown, Almadena Chtchelkanova, Kenneth N.C. Bray, Carolyn Kaplan, Martin Sichel, and Takanobu Ogawa for their help and for many fruitful discussions. Finally, we thank Rowena Ball, J. Craig Wheeler, Derek Bradley, and all of the anonymous reviewers for their careful reading and comments on the manuscript. Computing facilities were provided by the Laboratory for Computational Physics and Fluid Dynamics at the Naval Research Laboratory and DOD HPCMP program.

References

[1] A.M. Khokhlov, E.S. Oran, A.Yu. Chtchelkanova, J.C. Wheeler, Combust. Flame 117 (1999) 99–116.

[2] A.M. Khokhlov, E.S. Oran, G.O. Thomas, Combust. Flame 117 (1999) 323–339.

[3] A.M. Khokhlov, E.S. Oran, Combust. Flame 119 (1999) 400–416.

[4] E.S. Oran, A.M. Khokhlov, Phil. Trans. R. Soc. London Ser. A 357 (1999) 3539–3551.

[5] E.S. Oran, A.M. Khokhlov, Deflagrations, Hot Spots, and the Transition to Detonation, AIAA Fluid Dynamics Meeting, Paper AIAA-99-3771, AIAA, Reston, VA, 1999.

[6] A.M. Khokhlov, E.S. Oran, Adaptive Mesh Numerical Simulation of Deflagration-to-Detonation Transition: The Dynamics of Hot Spots, AIAA Fluid Dynamics Meeting, Paper AIAA-99-3439, AIAA, Reston, VA, 1999.

[7] E.S. Oran, A.M. Khokhlov, Numerical Simulation of Deflagration-to-Detonation Transition, 37th Aerospace Sciences Meeting, Paper AIAA-99-0965, AIAA, Reston, VA, 1999.

[8] V.N. Gamezo, E.S. Oran, A.M. Khokhlov, Formation of Induction Time Gradients for Detonation Initiation, 41st Aerospace Sciences Meeting, Paper 2003-1317, AIAA, Reston, VA, 2003.

[9] V.N. Gamezo, A.M. Khokhlov, E.S. Oran, Combust. Flame 126 (2001) 1810–1826.

[10] V.N. Gamezo, E.S. Oran, A.M. Khokhlov, Proc. Combust. Inst. 30 (2004) 1841–1847.

[11] E.S. Oran, V.N. Gamezo, A.M. Khokhlov, Effects of Boundary Layers and Wakes on Shock–Flame Interactions and DDT, 40th Aerospace Sciences Meeting, Paper 2002-0776, AIAA, Reston, VA, 2002.

[12] A.M. Khokhlov, V.N. Gamezo, E.S. Oran, in: Proc. 18th ICDERS, University of Washington, CD-ROM, ISBM 0-9711740-0-8, 2001.

[13] V.N. Gamezo, A.M. Khokhlov, E.S. Oran, Numerical Simulations of Ignition behind Reflected Shocks, Proceedings of the Second Joint Meeting of the US Sections of the Combustion Institute, Oakland, CA, 2001.

[14] V.N. Gamezo, A.M. Khokhlov, E.S. Oran, Effects of Boundary Layers on Ignition behind Reflected Shocks, Proceedings of the 18th ICDERS, University of Washington, ISBM 0-9711740-0-8, 2001.

[15] V.N. Gamezo, A.M. Khokhlov, E.S. Oran, Proc. Combust. Inst. 29 (2002) 2803–2808.

[16] V.N. Gamezo, T. Ogawa, E.S. Oran, Proc. Combust. Inst. 31 (2007), in press.

[17] V.N. Gamezo, A.M. Khokhlov, E.S. Oran, A.Y. Chtchelkanova, R.O. Rosenberg, Science 299 (2003) 77–81.

[18] V.N. Gamezo, A.M. Khokhlov, E.S. Oran, Phys. Rev. Lett. 92 (2004), 211102-1–4.

[19] V.N. Gamezo, A.M. Khokhlov, E.S. Oran, Astrophys. J. 623 (2005) 337–346.

[20] E.S. Oran, Proc. Combust. Inst. 30 (2004) 1823–1840.

[21] S.R. Brinkley Jr., B. Lewis, Proc. Combust. Inst. 7 (1959) 807–811.

[22] B. Karlovitz, in: W.R. Hawthorne, J. Fabri, D.B. Spalding (Eds.), Selected Combustion Problems, Butterworths, London, UK, 1954, p. 248.
[23] P. Urtiew, A.K. Oppenheim, Proc. R. Soc. London Ser. A 295 (1966) 13–28.
[24] A.J. Laderman, P.A. Urtiew, A.K. Oppenheim, Proc. Combust. Inst. 9 (1963) 265–274.
[25] A.K. Oppenheim, A.J. Laderman, P.A. Urtiew, Combust. Flame 6 (1962) 193–197.
[26] B. Lewis, G. von Elbe, Combustion, Flames, and Explosions of Gases, Academic Press, New York, 1987, p. 566.
[27] K.K. Kuo, Principles of Combustion, second ed., Wiley, New York, 2005, Chapter 4.
[28] J.H.S. Lee, Annu. Rev. Phys. Chem. (1977) 75–104.
[29] J.E. Shepherd, J.H.S. Lee, in: M.Y. Hussaini, A. Kumar, R.G. Voigt (Eds.), Major Research Topics in Combustion, Springer-Verlag, New York, 1992, p. 439.
[30] J.H.S. Lee, I.O. Moen, Prog. Energy Combust. Sci. 6 (1978) 359–389.
[31] O. Peraldi, R. Knystautas, J.H.S. Lee, Proc. Combust. Inst. 22 (1986) 1629–1637.
[32] S.B. Dorofeev, V.P. Sidorov, A.E. Dvoinishnikov, W. Breitung, Combust. Flame 104 (1996) 95–110.
[33] A. Teodorczyk, Biuletyn Instytutu Techniki Cieplnej Politechniki Warszawskiej 79 (1995) 145–178.
[34] S.B. Dorofeev, J. Phys. IV 12 (2002) 3–10.
[35] G.H. Markstein, Nonsteady Flame Propagation, Macmillan, New York, 1964, Chapter D.
[36] T. Scarinci, G.O. Thomas, Some Experiments on Shock–Flame Interactions, Report No. UCW/det905, Department of Physics, University of Wales, Aberystwyth (1990).
[37] T. Scarinci, J.H. Lee, G.O. Thomas, R. Bambrey, D.H. Edwards, Prog. Astronaut. Aeronaut. 152 (1993) 3–24.
[38] G.O. Thomas, C.J. Sands, R.J. Bambrey, S.A. Jones, in: Proceedings of the 16th ICDERS, 1997, pp. 2–5.
[39] G.O. Thomas, R. Bambrey, C. Brown, Combust. Theory Modelling 5 (2001) 573–594.
[40] R.D. Richtmyer, Comm. Pure Appl. Math. 13 (1960) 291.
[41] Y.Y. Meshkov, Instability of a Shock Wave Accelerated interface between Two Gases, Report No. NASA TTF-13, 074, NASA Tech. Trans. (1970).
[42] H.Gg. Wagner, in: Proc. International Specialists Conference on Fuel–Air Explosions, U. Waterloo Press, 1981, p. 77.
[43] R. Knystautas, J.H.S. Lee, I.O. Moen, H.Gg. Wagner, Proc. Combust. Inst. 17 (1978) 1235–1245.
[44] A.A. Boni, M. Chapman, J.L. Cook, J.P. Schneyer, in: L. Kennedy (Ed.), Turbulent Combustion, AIAA Reston, VA, 1978, p. 379.
[45] S.B. Dorofeev, A.V. Bezmelnitsin, V.P. Sidorov, J.G. Yankin, I.D. Matsukov, Proceedings of the 14th ICDERS, vol. 2, University of Coimbra, Coimbra, Portugal, 1993, pp. D2.4.1–D2.4.10.
[46] F. Carnasciali, J.H.S. Lee, R. Knystautas, Combust. Flame 84 (1991) 170–180.
[47] I.O. Moen, D. Bjerketvedt, A. Jenssen, Combust. Flame 61 (1985) 285–291.
[48] S.P. Medvedev, A.N. Polenov, S.V. Khomik, B.F. Gelfand, Proc. Combust. Inst. 25 (1994) 73–78.
[49] I.O. Moen, J.H.S. Lee, B.H. Hjertager, K. Fuhre, R.K. Eckhoff, Combust. Flame 47 (1982) 31–52.
[50] A.G. Merzhanov, Combust. Flame 10 (1966) 341–348.
[51] A.A. Borisov, Acta Astron. 1 (1974) 909–920.
[52] L.J. Zajac, A.K. Oppenheim, AIAA J. 9 (1971) 545–553.
[53] J.W. Meyer, A.K. Oppenheim, Combust. Flame 17 (1971) 65–68.
[54] Ya.B. Zeldovich, V.B. Librovich, G.M. Makhviladze, G.I. Sivashinsky, Astron. Acta 15 (1970) 313–321.
[55] J.H.S. Lee, R. Knustautas, N. Yoshikawa, Astron. Acta 5 (1978) 971–982.
[56] Ya.B. Zeldovich, Combust. Flame 39 (1980) 211–214.
[57] X.J. Gu, D.R. Emerson, D. Bradley, Combust. Flame 133 (2003) 63–74.
[58] A.K. Kapila, D.W. Schwendeman, J.J. Quirk, T. Hawa, Combust. Theory Modelling 6 (2002) 553–594.
[59] J.H. Chen, E.R. Hawkes, R. Sankaran, S.D. Mason, H.G. Im, Combust. Flame 145 (2006) 128–144.
[60] Ya.B. Zeldovich, B.E. Gelfand, S.A. Tsyganov, S.M. Frolov, A.N. Polenov, Prog. Astronaut. Aeronaut. 114 (1988) 99–123.
[61] A.M. Khokhlov, E.S. Oran, J.C. Wheeler, Combust. Flame 108 (1997) 503–517.
[62] C.J. Montgomery, A.M. Khokhlov, E.S. Oran, J.C. Wheeler, Combust. Flame 115 (1998) 38–50.
[63] D.L. Youngs, Physica D 12 (1984) 32–44.
[64] M.H. Emery, J.H. Gardner, R.H. Lehmberg, S.P. Obenschain, Phys. Fluids B 3 (1991) 2640–2651.
[65] X.L. Li, Q. Zhang, Phys. Fluids 9 (1997) 3069–3077.
[66] M. Brouillette, Annu. Rev. Fluid Mech. 34 (2002) 445–468.
[67] J.-F. Haas, Ph.D. thesis, California Institute of Technology, Pasadena, CA, 1984.
[68] J.-F. Haas, B. Sturtevant, J. Fluid Mech. 181 (1987) 41–76.
[69] J.M. Picone, J.P. Boris, Phys. Fluids 26 (1983) 365–382.
[70] J. M Picone, J.P. Boris, J. Fluid Mech. 189 (1988) 21.
[71] J. Yang, J., Ph.D. thesis, California Institute of Technology, Pasadena, CA, 1991.
[72] J.M. Picone, E.S. Oran, J.P. Boris, T.R. Young Jr., Prog. Astronaut. Aeronaut. 94 (1984) 429–448.
[73] V.T. Ton, A.R. Karagozian, F.F. Marble, S.J. Osher, B.E. Engquist, Theor. Comput. Fluid Dynam. 6 (1994) 161.
[74] G.A. Batley, A.C. McIntosh, J. Brindley, S.A.E.G. Falle, J. Fluid Mech. 279 (1994) 217–237.
[75] E.S. Oran, J.H. Gardner, Prog. Energy Combust. Sci. 11 (1985) 253–276.
[76] T.L. Jackson, M.G. Macaraeg, M.Y. Hussaini, J. Fluid Mech. 254 (1993) 579–603.
[77] G.P. Glass, G.B. Kistiakowsky, J.V. Mikhael, H. Niki, J. Chem. Phys. 42 (1965) 608–621.
[78] L.-K. Tseng, M.A. Ismail, G.M. Faeth, Combust. Flame 95 (1993) 410–426.
[79] R.A. Strehlow, C.D. Engel, AIAA J. 7 (1969) 492–496.

[80] S. Gordon, B.J. McBride, Computer Program for Calculation of Complex Chemical Equilibrium Compositions, Rocket Performance, Incident and Reflected Shocks, and Chapman–Jouguet Detonations, NASA SP-373 (1976).

[81] E.S. Oran, J.P. Boris, Numerical Simulation of Reactive Flow, Cambridge Univ. Press, New York, 2001.

[82] A.M. Khokhlov, J. Comput. Phys. 143 (1998) 519–543.

[83] T. Ogawa, E.S. Oran, AIAA J. (2006), in press.

[84] H. Mark, The Interaction of a Reflected Shock Wave with the Boundary Layer in a Shock Tube, Report No. TM-1418, NASA (1958).

[85] R.A. Strehlow, A. Cohen, J. Chem. Phys. 30 (1959) 257–265.

[86] L. Davies, The Interaction of a Reflected Shock Wave with the Boundary Layer in a Shock Tube and its Influence on the Duration of Hot Flow in the Reflected-Shock Tunnel—Part I, Report No. CP-880, British Aeronautical Research Council (1966).

[87] H. Kleine, V.N. Lyakhov, L.G. Gvozdeva, H. Grönig, in: Proc. 18th International Symposium on Shock Waves and Shock Tubes, Springer-Verlag, Berlin, 1992, pp. 261–266.

[88] L. Davies, J.L. Wilson, Phys. Fluids Suppl. I 12 (1969) 37–43.

[89] K. Matsuo, S. Kawagoe, K. Kage, Bull. Jpn. Soc. Mech. Eng. 17 (1974) 1039–1046.

[90] Y.S. Weber, E.S. Oran, J.P. Boris, J.D. Anderson Jr., Phys. Fluids 7 (1995) 2475–2488.

[91] Y. Takano, in: Proc. 18th International Symposium on Shock Waves and Shock Tubes, Springer-Verlag, Berlin, 1992, pp 869–874.

[92] G.J. Wilson, S.P. Sharma, W.D. Gillespie, in: Proc. 19th International Symposium on Shock Waves, Springer-Verlag, Berlin, 1995, pp. 439–444.

[93] D.A. Frank-Kamenetskii, Diffusion and Heat Transfer in Chemical Kinetics, Nauka, Moscow, 1967.

[94] Ya.B. Zeldovich, G.I. Barenblatt, V.B. Librovich, G.M. Makhviladze, The Mathematical Theory of Combustion and Explosions, Consultants Bureau, New York, 1985.

[95] A.M. Bartenev, B.E. Gelfand, Prog. Energy Combust. Sci. 26 (2000) 29–55.

[96] J.W. Meyer, J.W. Oppenheim, Proc. Combust. Inst. 13 (1971) 1153–1164.

[97] E.S. Oran, T.R. Young, J.P. Boris, A. Cohen, Combust. Flame 48 (1982) 135–148.

[98] D.J. Vermeer, J.W. Meyer, A.K. Oppenheim, Combust. Flame 18 (1972) 327–336.

[99] M.A. Liberman, G.I. Sivashinsky, D.M. Valiev, L.-E. Eriksson, in: Proceedings of the 20th ICDERS, Abstract 52, Montreal, 2005.

[100] N. Peters, Turbulent Combustion, Cambridge Univ. Press, New York, 2000.

[101] A.M. Khokhlov, E.S. Oran, J.C. Wheeler, Astrophys. J. 478 (1997) 678–688.

[102] S. Chandrasekhar, Astrophys. J. 74 (1931) 81–82.

[103] F.H. Shu, The Physical Universe: An Introduction to Astronomy, University Science Books, Mill Valley, CA, 1982, p. 128.

[104] W.D. Arnett, Astrophys. Space Sci. 5 (1969) 180–212.

[105] C.J. Hansen, J.C. Wheeler, Astrophys. Space Sci. 3 (1969) 464–474.

[106] K. Nomoto, D. Sugimoto, S. Neo, Astrophys. Space Sci. 39 (1976) L37–L42.

[107] K. Nomoto, R.K. Thielemann, K. Yokoi, Astrophys. J. 286 (1984) 644–658.

[108] S.E. Woosley, T.A. Weaver, Annu. Rev. Astron. Astrophys. 24 (1986) 205–253.

[109] A.M. Khokhlov, Astron. Astrophys. 245 (1991) 114–128.

[110] A.M. Khokhlov, E. Müller, P.A. Höflich, Astron. Astrophys. 270 (1993) 223–248.

[111] P.A. Höflich, A.M. Khokhlov, J.C. Wheeler, Astrophys. J. 444 (1995) 831–847.

[112] J.R. Boisseau, J.C. Wheeler, E.S. Oran, A.M. Khokhlov, Astrophys. J. 471 (1996) L99–L102.

[113] V.N. Gamezo, J.C. Wheeler, A.M. Khokhlov, E.S. Oran, Astrophys. J. 512 (1999) 827–842.

[114] W.A. Fowler, G.R. Caughlan, B.A. Zimmerman, Annu. Rev. Astron. Astrophys. 13 (1975) 69–112.

[115] S.E. Woosley, W.A. Fowler, J.A. Holmes, B.A. Zimmerman, At. Data Nucl. Data Tables 22 (1978) 371–441.

[116] F.-K. Thielemann, M. Arnould, J.W. Truran, in: E. Vangioni-Flam, J. Audouze, M. Casse, J.-P. Chieze, J. Tran Thanh Van (Eds.), Advances in Nuclear Astrophysics, Editions frontières, Gif-sur-Yvette, France, 1987, p. 525.

[117] W.R. Hix, F.-K. Thielemann, Astrophys. J. 460 (1996) 869–894.

[118] A.M. Khokhlov, http://www.arxiv.org/abs/astro-ph/0008463, 2000.

[119] M. Reinecke, W. Hillebrandt, J.C. Niemeyer, Astron. Astrophys. 386 (2002) 936–943.

[120] M. Reinecke, W. Hillebrandt, J.C. Niemeyer, Astron. Astrophys. 391 (2002) 1167–1172.

[121] A.M. Khokhlov, E.S. Oran, J.C. Wheeler, Combust. Flame 105 (1996) 28–34.

[122] E.S. Oran, in: P. Höflich, P. Kumar, J.C. Wheeler (Eds.), Cosmic Explosions in Three Dimensions, Cambridge Univ. Press, Cambridge, 2003, pp. 100–109.